

SPITZER IRS OBSERVATIONS OF CLASS I/II OBJECTS IN TAURUS:
COMPOSITION, TEMPERATURE AND THERMAL HISTORY OF THE CIRCUMSTELLAR ICES

G. ZASOWSKI¹, F. MARKWICK-KEMPER^{2,1}, DAN M. WATSON³, E. FURLAN^{4,5}, C.J. BOHAC³, C. HULL¹, AND J.D. GREEN³

Draft version February 2, 2008

ABSTRACT

We present observations of Taurus-Auriga Class I/II protostars obtained with the Spitzer InfraRed Spectrograph. Detailed spectral fits to the 6 and 15 micron features are made, using publicly-available laboratory data, to constrain the molecular composition, abundances, and levels of thermal processing along the lines of sight. We provide an inventory of the molecular environments observed, which have an average composition dominated by water ice with $\sim 12\%$ CO₂ (abundance relative to H₂O), $\gtrsim 2\text{--}9\%$ CH₃OH, $\lesssim 14\%$ NH₃, $\sim 4\%$ CH₄, $\sim 2\%$ H₂CO, $\sim 0.6\%$ HCOOH, and $\sim 0.5\%$ SO₂. We find CO₂/H₂O ratios nearly equivalent to those observed in cold clouds and lines of sight toward the galactic center. The unidentified 6.8 micron profile shapes vary from source to source, and it is shown to be likely that even combinations of the most common candidates (NH₄⁺ and CH₃OH) are inadequate to explain the feature fully. We discuss correlations among SED spectral indices, abundance ratios, and thermally-processed ice fractions and their implications for CO₂ formation and evolution. Comparison of our spectral fits to cold molecular cloud sight-lines indicate abundant prestellar ice environments made even richer by the radiative effects of protostars. Our results add additional constraints and a finer level of detail to current full-scale models of protostellar and protoplanetary systems.

Subject headings: stars: pre-main sequence — ISM: abundances — ISM: molecules — infrared: ISM — astrochemistry

1. INTRODUCTION

The chemical and thermal evolution of protostellar environments affects the spectral appearance of ices observed in the sequential stages of pre-main-sequence evolution (e.g. Willner et al. 1982; Gerakines et al. 1999; van Dishoeck 2006). The presence of the ice absorption features is often easily recognized, with the most common ones in the mid-infrared wavelength range found at 6.0, 6.8 and 15.2 μm , but the exact feature shapes depend strongly on the composition of the ice as determined by the initial condensation and subsequent thermal processing and UV irradiation. Mixing ices can cause wavelength shifts in the resonances of the individual components within the ice matrix (e.g. Ehrenfreund et al. 1999; Palumbo & Baratta 2000; Öberg et al. 2007), and differences in lattice structure caused by either radiation damage or thermal processing are spectroscopically identifiable (e.g. Hagen et al. 1981; Moore & Hudson 1992; Maldoni et al. 1998; Kouchi & Kuroda 1990).

The initial reservoir of star formation material, the diffuse ISM, is extremely ice-poor (e.g. Gillett et al. 1975; Whittet et al. 1997). Though often very cold ($T \lesssim 10\text{K}$), it is not dense enough to shield its dust grains, upon

which ices condense (e.g. Tielens & Allamandola 1987), from incident destructive photons. Only when cold molecular clouds of high density ($n_H \gtrsim 10^4 \text{cm}^{-3}$) are formed can interstellar ices survive and be observed. In the Taurus molecular cloud, for example, a well-known seat of starbirth, ices are observed towards background stars in quiescent regions unaffected by the newly-formed stars (e.g. Bergin et al. 2005; Knez et al. 2005; Whittet et al. 2007). These studies reveal absorptions attributable to H₂O, CO, and CO₂, as well as some less-constrained absorptions (e.g. the still unidentified band at 6.8 μm) due to presumably more complex species. The ice bands observed towards these field stars are smooth, indicating amorphous, unprocessed compounds, and low upper limits are placed on some species created by UV radiation (e.g. “XCN”; Gibb et al. 2004). These observations support the theory that molecular cloud ice chemistry is dominated by efficient cold grain surface reactions. The presence of some complex molecules (such as HCOOH, which can be formed at low temperatures; Keane 2001) demonstrates the potential complexity of these reactions and indicates that protostars are born into a pre-enriched chemical environment.

Young stellar objects (YSOs) deeply embedded in an infalling envelope, often referred to as Class 0 objects (Andre et al. 1993), display ice spectra generally similar in makeup to those of cold molecular clouds. However, surveys of embedded YSOs reveal a limited range of thermal processing in a number of sources, indicative of differences in YSO environment and temperature (e.g. Gerakines et al. 1999; Gibb et al. 2004). Studies of less-extinguished protostars (Class I in the classification of Lada 1987) find evidence of enhanced complex molecule formation (H₂CO, XCN, OCS, PAHs [polycyclic aromatic hydrocarbons]), crystallization, further thermal annealing, and ice matrix segregation

¹ Department of Astronomy, PO Box 400325, University of Virginia, Charlottesville, VA 22904-4325: gailis@virginia.edu, chat.hull@gmail.com

² Jodrell Bank Centre for Astrophysics, University of Manchester, Manchester, M13 9PL, UK: francisca.markwick-kemper@manchester.ac.uk

³ Department of Physics and Astronomy, University of Rochester, Bausch & Lomb Hall, PO Box 270171, 500 Wilson Blvd, Rochester, NY 14627-0171: dmw@pas.rochester.edu, joel@pas.rochester.edu, urgradcb@gmail.com

⁴ NASA Astrobiology Institute and Department of Physics and Astronomy, UCLA, 430 Portola Plaza, Los Angeles, CA 90095: furlan@astro.ucla.edu

⁵ NASA Postdoctoral Program Fellow

tion (see, e.g. Alexander et al. 2003; Keane et al. 2001; Ehrenfreund et al. 1998; Watson et al. 2004; Gibb et al. 2004; Boogert et al. 2004).

Finally, the least embedded Class II objects have seemingly accreted or dissipated most of their cold natal envelopes and have heated the outer layers of their dust disks above the sublimation temperature of astrophysical ices. These objects tend to show silicate dust *emission*, PAH emissions, and weak or nonexistent ice signatures (e.g. Forrest et al. 2004; Furlan et al. 2006), though some Class II edge-on systems have ice absorptions arising from the cold disk midplane (e.g. Pontoppidan et al. 2005; Furlan et al. 2007).

Differences in chemical and physical structure exist between high- and low-mass YSOs, where the boundary between high- and low-mass lies at a few M_{\odot} (van Dishoeck 2003). Some of these dissimilarities may be attributed to observational biases (low-mass YSOs are generally closer and can be better resolved), but others are likely to be dependent on the intrinsic nature of the object (e.g. the role of shocks, core temperature, and infall timescales). For example, low-mass YSO studies claim higher abundances of CO_2 , relative to H_2O (Boogert et al. 2004; Pontoppidan et al. 2007) and amorphous silicate dust (Watson et al. 2004), than surveys of more massive YSOs. This paper focuses on the relatively underexplored categories of low-mass Class I protostars and Class I/II transition objects (henceforth both groups will be collectively referred to as Class I/II objects) with ice absorptions by analyzing mid-infrared spectroscopy of 16 YSOs (1-3 Myr old; White & Ghez 2001) in the Taurus-Auriga star-forming region, observed with the InfraRed Spectrograph (IRS; Houck et al. 2004) on board the Spitzer Space Telescope (Werner et al. 2004). This sample helps complete our view of the ice evolutionary sequence from cold molecular clouds through warmer environments with protoplanetary disks. These low-mass, possibly early solar analogs are essential pieces to the puzzle of solar system formation.

Section 2 contains a short description of the sample, observations, and data reduction. In Section 3 we describe how the ice features are identified, isolated, and analyzed, and in Section 4 we look at trends seen in the feature optical depths. In Section 5 we derive the composition of the carriers of the primary ice absorptions and evaluate candidates for some of the less constrained features. In Section 6 we discuss composition and spatial distribution of the ices and place our observations in the context of pre-main-sequence evolution.

2. OBSERVATIONS

2.1. Target Sample Description

The Taurus-Auriga dark cloud is a nearby ($d \sim 140\text{pc}$; Bertout et al. 1999), low density ($n_{*} \sim 1\text{-}10\text{pc}^{-3}$; Gomez et al. 1993) star forming region containing predominantly young, low-mass protostars. It provides an opportunity to closely study low-mass star formation unaffected by the shocks and strong UV radiation associated with more massive protostars. Based on IRAS 25 and 60 μm photometry, an extensive sample of Class I/II objects selected from the list by Kenyon & Hartmann (1995) was observed with Spitzer’s IRS (Section 2.2); from this sample we chose for analysis the subset of 12 Class I and 4 Class II

objects (as classified in Kenyon & Hartmann 1995) with distinct ice features in regions of unsaturated, well-calibrated data. This set contains 5 spectra (IRAS 04016+2610, IRAS 04108+2803B, IRAS 04181+2654B, IRAS 04239+2436, DG Tau B) previously published by Watson et al. (2004). The IRAS SED points used in the original selection are insufficient to determine system inclination, and modeling by Furlan et al. (2007) indicates that our smaller sample spans a wide range of disk inclination angles, from nearly edge-on to face-on systems.

2.2. Observational Procedure and Data Reduction

Our sample was observed with Spitzer’s IRS as part of the *IRS Disks* project (PI: J. Houck/D. Watson; PID 2) during guaranteed time awarded to the IRS instrument team (2004 February-March). All of our targets were observed using the full 5–37 μm wavelength coverage, combining either the Short Low and Long Low (SL, LL; 5.2–14 μm , 14–38 μm ; $\lambda/\Delta\lambda \sim 90$) modules on the IRS, or the SL with the Short High and Long High (SH, LH; 10–19 μm , 19–37 μm ; $\lambda/\Delta\lambda \sim 600$) modules, depending on the expected flux levels.

Most (12) of the objects were observed using a small spectral map (3×2) rather than a single pointing; this strategy avoids the need for pointing peak-ups and allows, in principle, for a better reconstruction of the spectrum in cases of small mispointings. The three-step sequence was carried out in the dispersion direction, with the steps separated by three quarters (for the SL module) or one half (for the other modules) of the slit width. The two-step sequence corresponds to the normal IRS nod distance of one-third the slit length. The other 4 objects were observed in the IRS staring mode, using only the two nods along the slit. Observational details of all our targets are listed in Table 1.

We analyzed data from pipeline version S13, using the SMART package (Higdon et al. 2004). The standard *IRS Disks* reduction procedures, as well as any spectra requiring special treatment, are described in Furlan et al. (2006) and Furlan et al. (2007).

The uncertainty in each wavelength bin is taken to be half of the nod difference in flux level, except where this value is smaller than 1% of the flux. In those cases, the uncertainties are taken to be 1% of the flux in order to prevent underestimation. We estimate an absolute spectrophotometric accuracy of 5–10%.

2.3. IRS Spectra Description

As shown in Figure 1, the YSO mid-infrared spectra are dominated by broad solid state resonances, particularly those at 6.0, 6.8, 9.7, and 15.2 μm . Additional, but less pronounced, features are present in some spectra at 7.7 μm and as a broad band centered at 18 μm . Silicates are responsible for the broad 9.7 and 18 μm features, which can occur in either absorption (e.g. L1551 IRS 5) or emission (e.g. IRAS 04108+2803A).

The 6.0 μm feature is primarily due to the O-H bending mode of water ice, while the 6.8 μm feature remains largely unidentified, with CH_3OH and NH_4^+ (among others) as suggested carriers. The 7.7 μm absorption is generally attributed to solid CH_4 , and the 15.2 μm band is due to the O-C-O bending mode of solid CO_2 . A com-

plete inventory of absorption features identified in our spectra is contained in Table 2.

3. METHODS

3.1. Isolating the IR Features and Determining Optical Depths

3.1.1. YSO Spectra

The optical depth, τ , and shape of the individual absorption features under consideration are extracted from the astronomical spectra using a mathematical continuum fit. We make a cubic spline fit to the $\sim 5\text{--}20\ \mu\text{m}$ continuum of each spectrum using the following relatively feature-free regions: bluewards of the $6\ \mu\text{m}$ H₂O feature; between the unidentified $6.8\ \mu\text{m}$ feature and the onset of the $9.7\ \mu\text{m}$ silicate band; between the red wing of the silicate band ($\sim 14\ \mu\text{m}$) and the $15.2\ \mu\text{m}$ CO₂ feature; and redwards of the CO₂ feature—while ensuring that none of the feature wings are included in the continuum. We calculate the optical depth in the spectral features using $F_\lambda = F_{\lambda, \text{cont}} e^{-\tau_\lambda}$.

Because detailed modeling of the silicate mineralogy is beyond the scope of this paper, extraction of ice features blended with the $9.7\ \mu\text{m}$ silicate band (e.g. those of CH₃OH, NH₃, H₂O) is impracticable. However, the $18\ \mu\text{m}$ absorption feature in particularly silicate-rich spectra is much broader and shallower than the $15.2\ \mu\text{m}$ ice absorption it overlaps, so we can treat the silicate shape as a pseudo-continuum in order to isolate the ice absorption.

Additional steps are needed to extract small features in the $7\text{--}8\ \mu\text{m}$ range. The wide variation in $6.8\ \mu\text{m}$ and silicate absorption profile wings requires that each spectrum be treated individually. For objects not affected by the silicate feature bluewards of $8\ \mu\text{m}$, a straight-line continuum ($\sim 7.1\text{--}8\ \mu\text{m}$) is imposed to isolate any features. For objects affected by both the 6.8 and the $9.7\ \mu\text{m}$ features, two straight-line continua are imposed: one from $\sim 7.1\text{--}7.5\ \mu\text{m}$ and one from $\sim 7.5\text{--}8\ \mu\text{m}$ (Figure 2).

3.1.2. Laboratory Spectra

We use laboratory data from the Leiden University ice analog databases⁶ (Gerakines et al. 1995, 1996; Ehrenfreund et al. 1996, 1999; van Broekhuizen et al. 2006) to identify the composition and temperatures of the ices seen in our targets. In order to provide a direct comparison between the feature optical depths measured in the laboratory and those observed in the astronomical spectra, we removed a straight-line continuum from the laboratory data. For the wavelength ranges of interest, optical depths calculated using a straight-line continuum differ, on average, by less than half of a percent from those calculated using a more complicated cubic spline one. The wavelengths of the baseline ends are generally equal to the continuum points used in the astronomical spectra's spline fitting, with an occasional slight shift to ensure feature wings are excluded from the continuum. In Figure 3 we show the range of abundances contained in the Leiden database's non-irradiated H₂O:CH₃OH:CO₂ mixtures (T=10-185K); note that this plot does not represent the fraction of the database comprising other molecules (e.g. CH₄ and H₂OH) or UV-irradiated mixtures.

The temperatures given in this paper, except where otherwise noted, refer to laboratory conditions. Interstellar temperature barriers for crystallization, sublimation, and other physical processes are lower than their laboratory counterparts, due to the lower pressure and longer interaction timescales in interstellar space (e.g. Boogert et al. 2000). Particle shape corrections have not been applied to the laboratory spectra used in this broad analysis. The complex optical constants are unavailable for the database spectra used to model the more abundant ice mantle components, and such corrections would in any case be inappropriate for the annealed inhomogeneous mixtures used (Gerakines et al. 1999).

3.2. Spectral Fitting

To confirm the validity of using laboratory spectra to model *circumstellar* material, we estimate the total extinction A_V along the line of sight towards our YSOs using $A_V/\tau_{Si} \sim 17$ (Rieke & Lebofsky 1985). We find $A_V \sim 3\text{--}34$ for our total sample—and $A_V \sim 6\text{--}34$ for those objects without clear signs of dust emission contaminating the absorption feature—compared with the average extinction of $A_V \sim 1\text{--}5$ toward Taurus association stars (Myers et al. 1983). In addition, recent work has shown that in dense regions, this relation with a given τ_{Si} substantially underestimates A_V (Whittet et al. 1988; Chiar et al. 2007), so the total circumstellar extinction is likely to be even higher.

Thus, assuming that the foreground absorption towards the Taurus region is relatively low and that the spectral ice features result from material in the circumstellar environment, we can determine the ice composition and column densities of the circumstellar ice by fitting linear combinations of laboratory data to the observed IRS spectra. With the laboratory data described in Section 3.1.2, detailed spectral fitting is performed on the 6.0 and $15.2\ \mu\text{m}$ features using a standard χ^2 -minimization technique. The equation solved is

$$\tau(\lambda) = \sum a_i \tau_{\text{lab},i}(\lambda), \quad (1)$$

where the scale factors a_i of each component are the free parameters in the fit. To compare goodness-of-fit among various combinations, we use χ_ν^2 , the reduced χ^2 parameter. This is defined as $\chi_\nu^2 = \chi^2 / (n - m)$, where n is the number of spectral data points and m is the number of free parameters in the fit. Traditional statistics require $\chi_\nu^2 \sim 1$ for an acceptable fit, but our values are often significantly larger or smaller. Artificially small χ_ν^2 values can be caused by uncertainty overestimation or by poor signal-to-noise. Large values may be a result of uncertainty underestimation, unknown uncertainties in the laboratory spectra, or the existence of components not included in the fits. Therefore χ_ν^2 comparisons may be made to determine the best laboratory fit to a single spectrum; however, comparisons of goodness-of-fit among different YSO spectra are not necessarily valid. Quantities derived using a fitted spectral feature (e.g. processed fractions, column densities) were calculated using an average of all fits for that feature with a χ_ν^2 within 20% of the minimum.

3.3. Column Densities

⁶ <http://www.strw.leidenuniv.nl/~lab/databases/databases.htm>

To calculate column densities along the lines of sight to the YSOs, we use the relation (Alexander et al. 2003)

$$N(\text{cm}^{-2}) = \frac{\sum \tau_{\lambda} \Delta \lambda}{\lambda_{peak}^2 A}, \quad (2)$$

where $\Delta \lambda$ is the wavelength bin size, λ_{peak} is the wavelength of the feature's peak optical depth, and A (cm molec^{-1}) is the band strength as determined in the laboratory.

3.4. SED Spectral Index

To provide better resolution in evolutionary status than the simple Lada (1987) classification, we use the spectral index α (e.g. Kenyon & Hartmann 1995):

$$\alpha \equiv \frac{d \log \lambda F_{\lambda}}{d \log \lambda} \sim \frac{\log \lambda_2 F_{\lambda_2} - \log \lambda_1 F_{\lambda_1}}{\log \lambda_2 - \log \lambda_1}, \quad (3)$$

where we choose λ_1 and λ_2 to lie within featureless and well-calibrated parts of the spectrum but as much separated as possible (i.e. $\lambda_1 = 14.5 \mu\text{m}$ and $\lambda_2 = 30 \mu\text{m}$; Table 3). The slope of this section of the spectrum depends upon a variety of factors, including disk radius, total envelope density, outflow cavity opening angle, and inclination angle. With the exception of inclination angle, all of these factors depend upon the total dust column density in such a way that more dust produces a steeper SED slope, and models demonstrate that inclination angle effects are generally less significant than these other factors (Furlan et al. 2007). Thus small values for the spectral index α indicate a relatively blue or exposed stellar object, but with increasing α the spectrum becomes redder, indicating the YSO is more heavily embedded in dust.

4. OPTICAL DEPTH TRENDS

In Figure 4, we show correlations in the optical depths of the three strongest absorptions attributed to ices (at 6.0, 6.8, and 15.2 μm) in our YSO sample, in addition to a sample presented by Gibb et al. (2004). As seen by both studies, the 6.0 and 6.8 μm features are very closely correlated, with linear Pearson correlation coefficient $r = 0.96$ for our sample (Figure 4a). The peak ratio is $\tau_{6.8}/\tau_{6.0} \sim 0.96 \pm 0.03$, and the straight-line fit passes within 0.01 of the origin. Since the 6.0 μm band is primarily attributed to the bending mode of H_2O , this correlation indicates that the carrier(s) of the 6.8 μm band forms and evolves in a similar, polar environment.

There is only a loose correlation between the 6.0 μm and the 15.2 μm optical depths in our YSOs ($r = 0.7$, Figure 4b), reflected in a wide ratio range $\tau_{6.0}/\tau_{15.2} \sim 0.43$ -1.65. When the same ratios are calculated for the laboratory spectra, the spread is even wider (0.01-3.6), and only a small fraction fall within the range defined by the YSOs (Figure 3, filled circles); the 15.2 μm CO_2 feature is generally much stronger than the 6.0 μm water ice feature, independent of temperature. Mixtures dominated by H_2O provide most of the closest matches. In addition, there are two lab mixtures of nearly 1:1:1 $\text{H}_2\text{O}:\text{CH}_3\text{OH}:\text{CO}_2$ abundances (center of Figure 3) which have $\tau_{6.0}/\tau_{15.2}$ ratios comparable to the YSO ones but only after they have been heated to high temperatures ($T \gtrsim 125\text{K}$), nearing the ice sublimation points. The Leiden database has a scarcity of water-rich, CO_2 -poor ($\lesssim 20\%$) $\text{H}_2\text{O}:\text{CH}_3\text{OH}:\text{CO}_2$ mixtures in

the temperature range 10-180K, though based on this comparison, these compositions appear to be astronomically relevant. Because of the undersampling of compositions in this regime, we are not able to constrain the ice composition well from the $\tau_{6.0}/\tau_{15.2}$ ratio alone.

Despite being closely correlated with $\tau_{6.0}$, the 6.8 μm peak optical depth is even less correlated with the 15.2 μm depths ($r = 0.56$, Figure 4c). This indicates that much of the inherent scatter in the $\tau_{6.8}/\tau_{6.0}$ ratio is due to variations in the 6.8 μm feature among different lines of sight.

5. SPECTRAL FEATURE ANALYSES

5.1. The 6.0 μm Feature

Each YSO spectrum is fitted over the wavelength range 5.4-6.3 μm using the method described in Section 3.2 and the component set listed in Table 4. An example result is shown in Figure 5. Due to overlap with the unidentified 6.8 μm feature, the range above 6.3 μm was excluded in order to avoid imposing artificial structure on any fit residuals. These fits focus on identifying the constituents of the 6.0 μm feature— H_2O , H_2CO , HCOOH , and NH_3 , as described in the following subsections.

5.1.1. H_2O

Water is the least volatile and most abundant of the ices typically found along protostellar lines of sight. The strong 3 μm water ice resonance, which is used, when available, as a cleaner measure of H_2O abundance, is not included in the Spitzer IRS wavelength coverage, and the broad 13 μm libration feature is buried in the 9.7 μm silicate feature. Therefore, to calculate the H_2O column density, we use the 6.0 μm feature fit results along with equation 2 (summed over $\lambda=5.5$ -7 μm), with a band strength $A_{\text{H}_2\text{O}}$ of $1.2 \times 10^{-17} \text{cm molec}^{-1}$ for the $T \leq 50\text{K}$ water ice components and $A_{\text{H}_2\text{O}}=1.3 \times 10^{-17} \text{cm molec}^{-1}$ for the $T=120\text{K}$ one. These values are those of pure H_2O ice, though they are also suitable for concentrations of apolar dilutants of $\lesssim 30\%$ (Gerakines et al. 1995). The derived column densities $N(\text{H}_2\text{O})$ are listed in Table 5.

5.1.2. H_2CO and HCOOH

Many of the objects in our sample have additional absorptions centered around $\sim 5.8 \mu\text{m}$ that can be well-fit by a combination of H_2CO (formaldehyde) and HCOOH (formic acid) ices. Solid H_2CO is observed in many protostellar systems (e.g. Keane & Tielens 2003; Gibb et al. 2004) and plays an important role in the production of complex organic molecules (Schutte et al. 1993). H_2CO is difficult to detect independently in YSO Spitzer spectra; its 3.47 μm C-H stretch feature is beyond the wavelength range of the IRS, and its weaker 6.68 μm C=O stretch feature is blended with the 6.8 μm absorption, itself not well understood. The H_2CO column densities (Table 5) are derived using the observed integrated optical depth of the 5.8 μm feature (as determined from the spectral fits) and a band strength of $A_{\text{H}_2\text{CO}}=9.6 \times 10^{-18} \text{cm molec}^{-1}$ (Schutte et al. 1993).

Solid and gas-phase HCOOH has been detected in both low- and high-mass star-forming regions (e.g. Cazaux et al. 2003; Schutte et al. 1999; Bottinelli et al. 2004; Remijan et al. 2004). Within the IRS wavelength range, there are solid-state HCOOH absorptions

at 5.8 and 7.2 μm , and several in the 8-11 μm range (Bisschop et al. 2007). The latter ones are blended with the 9.7 μm silicate feature, but the 7.2 μm band, though intrinsically ~ 4 times weaker than the 5.8 μm resonance, is detectable and indeed has been tentatively identified in 6 of our 16 objects (Section 5.3). We have derived HCOOH column densities (Table 5) by integrating the observed optical depth of the 5.8 μm feature (as determined from the spectral fits) and using a band strength of $A_{\text{HCOOH}} = 6.7 \times 10^{-17} \text{ cm molec}^{-1}$ (Maréchal 1987).

5.1.3. NH_3

Solid NH_3 (ammonia) has mid-infrared features at 6.15 μm and 9.3 μm (e.g. Sandford & Allamandola 1993), blended with the 6 μm water ice and 9.7 μm silicate features, respectively. The effect on the 6 μm H_2O feature is negligible until the NH_3 concentration reaches $\sim 9\%$ (Keane et al. 2001). At higher concentrations, an excess appears around 6.15 μm on the red side of the 6 μm band in laboratory spectra, which fits well the broad 6 μm feature observed in many of our YSO spectra. Analyses of the 9 μm inversion mode resonance by Lacy et al. (1998) and Gibb et al. (2000) indicate that circumprotostellar NH_3 exists primarily in an H_2O -dominated matrix. Therefore, an $\text{H}_2\text{O}:\text{NH}_3$ (1:0.2) mixture, rather than pure NH_3 , is used in the spectral fits. Because no satisfactory band strength measurements for NH_3 in such a mixture exist, the upper limit NH_3 column densities (Table 5) are estimated by using the A of pure water ice for the $\text{H}_2\text{O}:\text{NH}_3$ mixture and extrapolating the column density of NH_3 based on its fractional abundance in the final fit.

5.1.4. PAHs

After contributions due to H_2O , H_2CO , HCOOH, and NH_3 are subtracted, small residuals in the 6.1-6.4 μm range, varying in strength, shape, and peak position, are observed in 11 of the sample's 16 YSOs. PAH absorption has been suggested as a candidate for the 6.2-6.3 μm feature observed in many massive protostars (Schutte et al. 1996). Using the average interstellar PAH spectrum compiled by Hony et al. (2001) as a reference, we examined the peak position and widths of the YSO residuals. Of the objects within our sample with excess absorptions peaking between 6.2 and 6.3 μm , only three (IRAS 04361+2540, DG Tau B, and HL Tau) have an excess with a width similar to that seen in the PAH spectrum, and none of these three match the PAH feature in shape and peak position. Though the PAH relative band strengths often depend upon molecular environment and ionization level, the broad 7.5-9 μm complex and the 6.2 μm feature are consistently observed at comparable strength in astronomical environments (Hony et al. 2001), yet we find no correlation in the YSO spectra between the 6.2 and 7.7 μm optical depths—the ratios range from 0-7.5. Moreover, the prominent but narrow PAH peak at 11.3 μm (consistently $\sim 1.4\times$ as strong as the 6.2 μm peak; Chan et al. 2000; Hony et al. 2001) and the lesser ones at 12.7, 13.5, and 14.3 μm are not observed in the YSO data. Thus it is unlikely that PAHs contribute significantly around 6.2-6.3 μm .

5.2. The 6.8 μm Feature

Though the 6.8 μm interstellar absorption band was discovered nearly 30 years ago (Puetter et al. 1979), its identification remains ambiguous and inconclusive. Species ranging from hydrocarbons to alcohols to carbon dust have been proposed to contribute to the feature in a variety of sources (see Keane et al. 2001). Here we focus on CH_3OH and NH_4^+ —the candidate carriers most commonly accepted as explaining at least part of the absorption (e.g. Boogert & Ehrenfreund 2004).

5.2.1. CH_3OH

The position of the 6.8 μm feature coincides with the C-H deformation mode of alcohols, and of these, methanol is the most likely to be found in interstellar abundance. Theoretical models of ice processes predict the creation of solid methanol through the sequential hydrogenation of CO ice which has been accreted from the gas phase onto dust grains (Tielens & Charnley 1997). The presence of methanol ice in interstellar and protostellar environments is observationally supported by detection of its own resonances—e.g. the C-H stretching mode at 3.54 μm (Grim et al. 1991) and the C-O stretch at 9.7 μm (Gibb et al. 2000)—as well as signatures of its interactions with other molecules (especially CO_2 ; e.g. Ehrenfreund et al. 1998).

Our sample spectra do not contain the NIR wavelengths of CH_3OH 's multiple stretching modes, and the 9.7 μm resonance is blended with the silicate absorption. However, constraints on the CH_3OH abundance can be derived using the 15.2 μm CO_2 band, as the interaction of CH_3OH with CO_2 causes a shoulder near 15.4 μm (Sections 5.4 and 6.1). The relative strength of the 15.4 μm shoulder implies that at most 50% of the 6.8 μm feature is due to CH_3OH in a CO_2 matrix, although CH_3OH unmixed with CO_2 could be present to provide additional absorption at 6.8 μm . Since CH_3OH is thought to form in a hydrogenated environment, the assignment of at least part of the 6.8 μm absorption to this molecule is then supported by the close correlation of the 6.0 and 6.8 μm optical depths (Section 4).

5.2.2. NH_4^+

The ion NH_4^+ was proposed as the carrier of the 6.8 μm band by Grim et al. (1989), and since then, this proposal has achieved varying levels of success (e.g. Schutte et al. 1996; Keane et al. 2001; Schutte & Khanna 2003). The ion can be produced in the laboratory by the acid-base reaction $\text{HNCO} + \text{NH}_3 \rightarrow \text{OCN}^- + \text{NH}_4^+$ (Keane 1997) or in UV-irradiated $\text{H}_2\text{O}:\text{CO}:\text{NH}_3$ mixtures (as in Figure 6).

NH_4^+ has expected counter-ion features at 4.62 μm (OCN^-) and 6.3 and 7.41 μm (HCOO^- , produced by photolysis). 4.62 μm is too blue for IRS data and the 7.41 μm signature is too weak to be conclusively identified in our data. However, some of our sample objects do have a small excess absorption near 6.3 μm (Section 5.1.4), which is unlikely to be attributable to PAHs. It may instead be due to HCOO^- , indicating photolysis and subsequent warming of a polar ice containing NH_3 . We use the ratios of the laboratory 6.3 μm (HCOO^-) and 6.8 μm (NH_4^+) peaks ($\tau_{6.8}/\tau_{6.3} \sim 1.7$ after the H_2O feature is removed), along with the equivalent widths of the YSO and laboratory features, to estimate the NH_4^+ contribution to the 6.8 μm feature. Using this method, we find

that, within our sample, 6-58% of the 6.8 μm feature can be attributed to NH_4^+ (HL Tau is an outlier whose particularly large 6.3 μm excess indicates $\lesssim 91\%$ of its 6.8 μm feature may be due to NH_4^+ using this method).

5.2.3. Fits and Summary

Figure 6 shows a comparison of the 6.8 μm features, after subtraction of the red wing of the 6 μm H_2O features, with a variety of 6.8 μm candidate laboratory spectra, all rebinned to the resolution of the observations. The bottom two lab spectra have $\text{CH}_3\text{OH}/\text{H}_2\text{O}$ abundance ratios of 100 and 0.1, and the vertical dotted lines indicate the peak positions of these mixtures. The relative amount of CH_3OH present affects the peak substructure. While in some cases the YSO peak positions and relative strengths closely resemble the laboratory data (e.g. IC 2087 IR and IRAS 04239+2436), in others there is no correlation at all (e.g. IRAS 04169+2702). The abundance of CH_3OH (relative to H_2O) has been found to vary by almost an order of magnitude among different protostellar lines of sight (e.g. Pontoppidan et al. 2003; Gibb et al. 2004), which may partly explain the observed variety of peak substructures.

The third laboratory spectrum in Figure 6 is a $\text{H}_2\text{O}:\text{CO}:\text{NH}_3$ deposit, irradiated to create NH_4^+ and subsequently warmed to from 10 to 165K. The irradiated spectrum at 10K peaks 0.1 μm bluewards of our sample's bluest feature; in order to align with any of the observed profiles, the irradiated mixture must be heated to near the H_2O sublimation temperature, as the sublimation appears to cause the redward peak shift (Schutte et al. 1996). Moreover, the width of the NH_4^+ feature is too narrow ($\sim 0.25 \mu\text{m}$) to account for the entire 6.8 μm feature widths observed towards each YSO (average $\sim 0.4 \mu\text{m}$). Even if multiple NH_4^+ laboratory spectra at various temperatures are combined in order to reproduce the observed feature width, the resultant peak position remains too blue to match the YSO data.

Noting that many of the YSO 6.8 μm features share characteristics with the profiles of both CH_3OH (triple peaks, 7 μm shoulder) and NH_4^+ (asymmetric peak near 6.75 μm), we attempted fitting them with a combination of the laboratory components. While no remarkably good fits were achieved, there emerged a general trend that equal contributions from NH_4^+ and from CH_3OH in a water-dominated matrix, with varying amounts of nearly-pure CH_3OH intermixed, came closest to reproducing many of the YSO feature width-to-depth ratios (i.e. mixtures of irradiated NH_3 , $\text{CH}_3\text{OH}/\text{H}_2\text{O} \sim 0.1$, and $\text{CH}_3\text{OH}/\text{H}_2\text{O} \sim 100$ in the approximate ratios 1:1:0 to 1:1:1). However, the overall 6.8 μm astronomical feature shapes could not be well-matched in terms of either peak alignment or subpeak relative strengths.

Based on this work, we conclude that we cannot rule out NH_4^+ and CH_3OH as contributors each of at most $\sim 50\%$ to the 6.8 μm band, but we emphasize that even the 50/50 combinations do not reproduce the overall feature shapes. Studies of this feature performed with higher-resolution ISO-SWS observations (e.g. Keane et al. 2001; Schutte et al. 1996) find a similar variety of structure and peak positions, confirming that it may be difficult or physically impossible to adequately explain the feature using the same set of components for

all sight-lines.

5.3. The 7-8 μm Range

Because of the uncertainties due to the low resolution and low signal-to-noise of the 7-8 μm optical depth spectrum, as well as the inherent narrowness of the 7-8 μm features, we did not attempt to fit the shape of the spectral features with laboratory profiles but rather focused on detection of the 7.25 μm HCOOH , $\sim 7.6 \mu\text{m}$ SO_2 , and 7.7 μm CH_4 features.

5.3.1. HCOOH

The 7.25 μm HCOOH band is intrinsically ~ 4 times weaker than the 5.85 μm band (Bisschop et al. 2007). Based on the amount of HCOOH in the fitted spectra in Section 5.1, the expected 7.25 μm optical depths in the YSO spectra are $\lesssim 0.02$. Indeed, we do observe small features at 7.25 μm in 6 of our 16 objects. It should be noted, however, that the strength of these do not correlate with the HCOOH column densities derived from the spectral fits and the stronger 5.85 μm feature ($r = 0.06$); also, there are other species with weak signatures very close to this wavelength (e.g. HCOO^- and HCONH_2 ; Schutte et al. 1999). As the optical depth profiles here are neither strong nor resolved enough to conclusively distinguish among these species' signatures, these HCOOH detections must remain tentative.

5.3.2. CH₄ and SO₂

In 13 of our 16 objects, we observe a feature near 7.7 μm , where the (ν_4) C-H deformation mode of CH_4 is expected. Laboratory studies have shown that this resonance's position and width are strongly dependent on the molecular environment, becoming blue-shifted (as far as 7.64 μm) and broader when mixed with a variety of other ices, including H_2O , CO , CH_3OH , and CO_2 (Boogert et al. 1997). In addition, there is the possibility of blending with a nearby SO_2 feature.

The 7.58 μm S-O stretching band of SO_2 has been shown to vary its peak position from 7.45-7.62 μm , depending on the temperature and the molecular environment (Boogert et al. 1997). In order to disentangle absorption due to SO_2 and CH_4 , we fit each YSO's 7.45-8 μm wavelength range with two Gaussian curves, allowing the peak of one (representing SO_2) to shift between 7.45-7.62 μm and constraining the other peak (CH_4) to 7.62 μm or larger. A Gaussian approximation was chosen because both the SO_2 and CH_4 profiles are too narrow, compared with the IRS resolution, to evaluate any substructure. In many cases, a single Gaussian was sufficient, indicating a single, distinct feature of either SO_2 or CH_4 , depending on peak position. Of our 16 YSOs, 7 show only a 7.7 μm feature with little or no asymmetrical excess, 3 only have a distinct feature peaking within the SO_2 range, 4 show both distinct features, and 2 show a broad absorption with additional peaks within the SO_2 range (i.e. fit by overlapping Gaussians). Using the range of laboratory feature FWHMs (full widths at half maximum) measured by Boogert et al. (1997), we find that in 4 of the 9 objects with either distinct features or a Gaussian fit in the 7.45-7.62 μm range, the feature width is too narrow ($\Delta\lambda \lesssim 0.06 \mu\text{m}$) to be attributed to solid SO_2 . These may be due to random noise creating an

apparent peak, or to CH₄ gas lines found between ~ 7.4 – $8 \mu\text{m}$. SO₂ also has gas lines in this region, but these are very weak (Boogert et al. 1997). For the 5 remaining features, we use equation 3.3 with a band strength $A_{\text{SO}_2} = 3.4 \times 10^{-17} \text{cm molec}^{-1}$ (Khanna et al. 1988) to determine the SO₂ column density; for the other objects, an upper limit to N(SO₂) is determined (Table 5).

Of the 13 objects with a distinct $7.7 \mu\text{m}$ CH₄ feature or Gaussian fit, 7 have FWHMs comparable to those observed in laboratory mixtures (Boogert et al. 1997), particularly in those mixtures where CH₄ and either H₂O, CH₃OH, or NH₃ exist in roughly equal abundance. The remaining 6 objects have wider features, which may be explained by variations in temperature or ice mantle composition along the line of sight. To determine the column density of CH₄ towards each YSO, we use equation 3.3 with a band strength $A_{\text{CH}_4} = 7.3 \times 10^{-18} \text{cm molec}^{-1}$ (pure CH₄; discussion in Boogert et al. 1997) and integrate the optical depth between 7.6 – $7.9 \mu\text{m}$. Upper limit estimates for the 3 non-detections are provided by the noise in the spectrum (Table 5).

5.4. The 15.2 μm Feature

Double-peaked structure in the $15.2 \mu\text{m}$ feature, often observed in systems with an exposed source of heating and radiation (such as Class I objects) is associated with the dual peaks of the degenerate ν_2 bending mode in pure CO₂ ice. This structure becomes less pronounced or disappears altogether when the apolar CO₂ molecules are embedded in an H₂O-rich polar matrix (e.g. Ehrenfreund et al. 1999). Thus the presence of a double-peaked feature indicates that thermal processing has occurred, segregating the CO₂ from the polar matrix. The broad shoulder on the red side of the absorption, centered around $15.4 \mu\text{m}$, has been attributed to CO₂ interactions with other molecules, particularly CH₃OH, and the strength and shape of the shoulder depend on both temperature and relative abundances (e.g. Dartois et al. 1999). Studies suggest that solid CO₂ is formed by oxidation of CO ice (e.g. Tielens & Hagen 1982; Ruffle & Herbst 2001), so the co-existence and interaction with solid CH₃OH (also formed from CO; Tielens & Charnley 1997) is not unexpected.

In the fits, made for the high-resolution spectra⁷ between 14.7 and $16 \mu\text{m}$, we include cold (10 – 30K) deposits of H₂O:CO₂, pure CO₂, and an irradiated deposit of CO:H₂O, as well as warmer ($\gtrsim 100\text{K}$) mixtures of H₂O:CH₃OH:CO₂ (Table 6). The cold mixtures containing H₂O are used to estimate the contribution from non-processed material along the line of sight. The warmer H₂O:CH₃OH:CO₂ spectra represent ices which have been warmed and have undergone the chemical and physical changes, including segregation of the CO₂, resulting from that processing. The pure CO₂ component, though measured at 10K , does not greatly differ in shape until sublimation at $\sim 80\text{K}$ and is here used as a measure of segregated, highly-processed ice.

Using a single component fit, we find that a nearly equal-parts mixture of H₂O:CH₃OH:CO₂ at temperatures of $\gtrsim 100\text{K}$ provides the lowest- χ^2_ν fit to the observed YSO $15.2 \mu\text{m}$ absorption bands, in accordance

with previous results for more massive protostars (e.g. Ehrenfreund et al. 1999; Gerakines et al. 1999). Where present, the dual peak positions align, and the approximate strength of the $15.4 \mu\text{m}$ shoulder is replicated. The fit improves, however, by an average of $\sim 50\%$ of χ^2_ν , when we allow multiple components (Figure 7). The combination of these additional components reproduces the relative peak strengths, the inter-peak dip depth, and the shape of the $15.4 \mu\text{m}$ shoulder without requiring a specific single temperature.

Our multicomponent fits indicate that for our YSO sample, a smaller amount of CH₃OH ($\sim 14\%$) at lower temperatures is sufficient to account for the observed $15.4 \mu\text{m}$ shoulder, and equal parts H₂O, CO₂, and CH₃OH exist at high temperatures, higher than those identified by e.g. Ehrenfreund et al. (1999), when the CO₂ has at least partly migrated out of the matrix. Laboratory mixtures at these higher temperatures that also contain the smaller fractions of CH₃OH have an asymmetrical dual peak that is not observed in the YSO spectra; mixtures with H₂O, CH₃OH, and CO₂ in a 1:1:1 ratio at lower temperatures show a stronger shoulder at $15.4 \mu\text{m}$ (relative to the main peak) as well as a nearly-single peak at $15.2 \mu\text{m}$. While the cold-grain formation and expected abundances of CH₃OH are not tightly-constrained (e.g. Tielens & Whittet 1996; Keane et al. 2001, and references therein), the generally-higher abundances observed towards high-mass protostars are evidence that warmer environments may be conducive to additional CH₃OH production. This is consistent with the stronger $15.4 \mu\text{m}$ shoulders observed towards massive protostars (compared with low-mass ones; e.g. Ehrenfreund et al. 1998; Boogert et al. 2004), and the equal-parts H₂O:CH₃OH:CO₂ mixtures required to fit them. Most of our YSO fits are further improved by including the very cold ($\sim 30\text{K}$) CO:H₂O layer, representing absorption along the line of sight due to cold material, affected by the region’s radiation field but too distant or too shielded from the central source to have undergone thermal heating.

We have calculated the total CO₂ column density (Table 5) observed along each YSO line of sight using equation 2. The exact band strengths of the laboratory mixtures used in the $15.2 \mu\text{m}$ fits are undetermined. The fitting results indicate that the vast majority of the CO₂ ice resides alongside H₂O ice, so we use a band strength of $1.5 \times 10^{-17} \text{cm molec}^{-1}$ (Gerakines et al. 1995), which is appropriate for the $15.2 \mu\text{m}$ absorption from a H₂O:CO₂ 1.6:1 ice. The observed optical depth spectra were integrated between 14.7 – $16 \mu\text{m}$. We use the relative contributions of each fitting component to estimate the column density of solid CO₂ in each stage of thermal processing (Table 7): radiation-only (10 – 30K , “cold”), some thermal heating (“warm”), and CO₂ segregation. We have also estimated the column density of solid CH₃OH embedded in CO₂ using the the CH₃OH abundance and relative contribution of each laboratory fit component (Table 5).

6. DISCUSSION

6.1. Ice Composition and Chemistry

6.1.1. CO₂ vs H₂O Abundances

From the derived column densities (Table 5), we find $N(\text{CO}_2)/N(\text{H}_2\text{O}) \sim 0.12 (\pm 0.04)$. This is

⁷ The low-resolution spectra are insufficient to resolve any structure which might be present.

compared in Figure 8 with the average value $N(\text{CO}_2)/N(\text{H}_2\text{O}) \sim 0.17 (\pm 0.03)$ derived for previous samples of many different sight-lines (Gerakines et al. 1999; Nummelin et al. 2001; Gibb et al. 2004; Knez et al. 2005; Alexander et al. 2003), and the slightly higher value $N(\text{CO}_2)/N(\text{H}_2\text{O}) \sim 0.3$, with large scatter, reported by Boogert et al. (2004) and Pontoppidan et al. (2007). These studies used the band strength of *pure* CO_2 when deriving the column densities, whereas we chose the more physical A_{CO_2} of an $\text{H}_2\text{O}:\text{CO}_2$ mixture. If we instead use the pure CO_2 value, we find $N(\text{CO}_2)/N(\text{H}_2\text{O}) \sim 0.16 (\pm 0.04)$, nearly equivalent to the majority to the previous studies, which include high- and low-mass YSOs, background field stars sampling molecular clouds, and galactic center sight-lines sampling diffuse interstellar material and molecular clouds. This consistency indicates that the dominant formation mechanisms for H_2O and CO_2 do not strongly depend on the characteristics or even presence of an embedded thermal or radiative source (c.f. e.g. Gerakines et al. 1999; Whittet et al. 2007).

The dashed line in Figure 3 identifies the locus of compositions with $\text{CO}_2/\text{H}_2\text{O} = 0.12$. It passes near those mixtures with $\tau_{6.0}/\tau_{15.2}$ most closely matching those of our YSO sample, and also through the underrepresented compositional space, as described in Section 4. Despite this gap in the laboratory data, we have achieved good fits to the 6.0 and 15.2 μm features using combinations of ice mixtures, demonstrating that significant structure exists in the ice composition along the line of sight; this structure is unconstrainable by simple total sight-line abundance ratios.

Within our YSO sample, we find slight positive correlations between the 14.5-30 μm spectral index α and the abundance of solid H_2O and CO_2 (Figure 9)—presumably, the higher dust column densities of more deeply embedded objects shield the ice-coated grains from the UV and thermal radiation of the protostellar object. Interestingly, the $N(\text{CO}_2)/N(\text{H}_2\text{O})$ relation shows a increase at lower α , suggesting that the CO_2 supply is enhanced in less-embedded regions or that H_2O is preferentially destroyed in those same regions. Examining the ice database H_2O and CO_2 spectra, we see that the sublimation temperature of solid H_2O is $\gtrsim 40\text{K}$ higher than that of pure CO_2 ice. Although CO_2 molecules embedded in a polar matrix may become “trapped” and able to survive to temperatures nearing the sublimation limit of H_2O , the thermal destruction of H_2O before CO_2 is unlikely. However, photodissociation of H_2O can produce radicals (e.g. OH) which themselves can react to form CO_2 on the grain surface (e.g. $\text{CO} + \text{OH} \rightarrow \text{CO}_2$; Allamandola et al. 1988). Ehrenfreund et al. (1999) observed that, in irradiated laboratory $\text{H}_2\text{O}:\text{CH}_3\text{OH}:\text{CO}_2$ mixtures, the CO_2 eventually reaches a constant abundance level due to an equilibrium between destruction and formation. The dominant formation mechanism of CO_2 in interstellar space is not yet determined conclusively, but some of the reaction pathways, including that given above, have activation barriers which will become more surmountable in warmer, more exposed environments (e.g. Ruffle & Herbst 2001; van Dishoeck & Blake 1998). Thus it is possible we see slightly enhanced CO_2 abundance (relative to H_2O) due to greater UV radiation and higher temperatures in regions of lower dust column

density.

6.1.2. HCOOH and CH_3OH vs H_2O Abundances

In Figure 10, we show the relationships between the column densities of H_2O , HCOOH , and CH_3OH intermixed with CO_2 . Apart from one outlier at $N(\text{H}_2\text{O}) \sim 1.1 \times 10^{19} \text{cm}^{-2}$ (L1551 IRS 5), the trend of increasing $N(\text{HCOOH})$ with increasing $N(\text{H}_2\text{O})$ ($r = 0.61$) supports laboratory experiments demonstrating that the most likely formation environments of solid HCOOH are those that also produce H_2O ice, through either radiative processing or cold surface reactions (Bisschop et al. 2007). We find a range of HCOOH abundances from 0-2% (relative to H_2O), well within the $\lesssim 5\%$ range observed in (mostly-massive) protostellar sight lines (Bisschop et al. 2007). It is known that the $N(\text{CH}_3\text{OH})/N(\text{H}_2\text{O})$ abundance varies greatly from source to source (e.g. Boogert & Ehrenfreund 2004), consistent with the large scatter in our observed ratios (see Section 6.1.4).

6.1.3. CH_4 vs H_2O Abundances

Laboratory studies of solid CH_4 indicate that it can be formed by a variety of processes—including UV photolysis of CH_3OH ices (Allamandola et al. 1988) and grain-surface hydrogenation of carbon (Tielens & Hagen 1982)—and the resulting absorption profile has characteristics unique to its formation and environment (Boogert et al. 1997). Unfortunately, as described in Section 5.3.2, the low signal and resolution of the observed profiles preclude spectral fitting or detailed shape comparisons with laboratory profiles; however, the broad range of peak positions and widths implies that the CH_4 environments vary across the sample.

Solid CH_4 has generally been found with an abundance $\sim 0.5\text{-}4\%$ relative to H_2O (Boogert et al. 1996; Gibb et al. 2004). We find a range of abundances from $\sim 0.3\text{-}8\%$, with an average of 2.6% and a single outlier (IRAS 04154+2823) at 23% (Figure 11). The high values ($>4\%$) may be partially due to additional absorptions unresolvable at the SL-module resolution, such as gas-phase CH_4 lines, or to matrix-dependent variations in band strength. Hudgins et al. (1993) found that the band strength for the 7.7 μm CH_4 feature may vary by as much as a factor of 2.8 between mixtures dominated by H_2O and by CO . We used the value for pure CH_4 , which lies approximately midway between the two extremes, but without the ability to resolve substructural differences among the various mix profiles, it is impossible to determine just how significant is the effect of differing molecular environments on the final feature. The profiles yielding the highest $N(\text{CH}_4)$ measurements are among the broadest, and their peak positions are consistent with CO -rich mixtures, which have the largest intrinsic band strength and could reduce the 8% abundance to 4.4%. Because these peak positions are not unique to the CO mixtures, higher-resolution observations are required to conclusively constrain the matrix makeup.

6.1.4. Evidence for CH_3OH Abundances—6.8 μm and 15.4 μm Features

As noted in Section 5.4, our fits to the 15.2 μm profiles provide evidence for solid CH_3OH intermixed with

CO₂—the CH₃OH:CO₂ complex peaking near 15.4 μ m provides the observed long-wavelength shoulder. In the laboratory spectra indicated by plus signs in Figure 12 (wherein the 6.8 μ m feature is due solely to CH₃OH), we observe a relationship between the strength of the 15.4 μ m shoulder and the 6.8 μ m feature. The astronomical data, indicated by filled circles, show that the CO₂ 15.4/15.2 μ m τ -ratios lie within the mid-range of the laboratory spectra ratios. However, the peak 6.8 μ m depths are either equal to or significantly greater than the laboratory 6.8 μ m depths. This could be understood if only a small fraction of the CH₃OH along the line of sight is embedded in a CO₂ matrix or if there are significant contributions to the 6.8 μ m feature ($\gtrsim 50\%$) from one or more different species.

We use the laboratory fits to the 15.2 μ m feature to estimate the column density of solid CH₃OH intermixed with CO₂ as 30-56% with respect to CO₂ (high-resolution observations only), corresponding to 2-9% with respect to H₂O. If we assume that $\lesssim 50\%$ of the 6.8 μ m feature is due to CH₃OH (Section 5.2.3), we estimate total CH₃OH abundances of $\lesssim 5$ -17% with respect to H₂O (all observations, with two outliers, IRAS 04108+2803A and IRAS 04181+2654B, at 32 and 28%; Table 5). Consistent with the detection of solid CH₃OH with abundances (relative to H₂O) up to $\sim 25\%$ towards low-mass YSOs (Pontoppidan et al. 2003), our data support the presence of a significant CO₂-poor H₂O:CH₃OH ice component, varying greatly in abundance among the sources.

6.2. Segregation of CO₂ Ice

In the colder parts ($\lesssim 20$ K) of a star-forming region, well-removed from the hot cores and embedded protostars or buried in dense clumps, dust grains accumulate an apolar ice mantle (solid CO, N₂, O₂) on top of their polar (H₂O-dominated) one. As the temperature increases closer to the star or on the exposed parts of the disk, the most volatile ices sublime and the remaining ices can interact to form both molecular complexes and new species (e.g. CH₄, NH₃, CO₂; Boogert et al. 1997; Ehrenfreund et al. 1998). As the dust grains and ice mantles are heated further, laboratory studies show that the CO₂ can migrate and aggregate, either as a surface layer or in bulk clumps within the matrix (e.g. Sandford & Allamandola 1990; Ehrenfreund et al. 1999). These processes destabilize the CO₂:CH₃OH complexes and reduce the 15.4 μ m shoulder; the spectrum becomes dominated by the twin peaks of pure CO₂ (though the bluer 15.1 μ m one is characteristically stronger and broader). Figure 13 demonstrates that this process can happen rather abruptly.

A double-peaked structure (15.1, 15.25 μ m) with a shoulder (15.4 μ m) is evident in 6 of the 9 high-resolution observations of the 15.2 μ m CO₂ absorption, though all 9 show deviations from the smooth, unprocessed Taurus cloud profiles (Whittet et al. 2007; Bergin et al. 2005; Knez et al. 2005). The variation within our sample is shown in Figure 14. In agreement with Boogert et al. (2004) (and in contrast with Nummelin et al. 2001), we have found evidence in all of our YSO spectra for moderate-temperature thermal processing ($\lesssim 100$ K—CO₂ warmed but not segregated) in the low-mass envelopes. However, unlike Boogert et al. (2004), we also find evidence for high-temperature processing—5 of the 9

objects have 15.2 μ m profiles entirely dominated by processed ices in which a significant fraction (~ 20 -40%) of the CO₂ has segregated from the polar formation matrix.

We can also derive the mass distribution of CO₂ ice as a function of temperature. Using the behavior of laboratory ice analogs, we define limiting temperatures for each stage of YSO ice processing; when combined with full-SED radiative transfer models, these temperatures will become physical distances, leading to the geometrical mass distribution of CO₂-coated grains. In Figure 13, we have illustrated the onset of CO₂ segregation at a laboratory temperature of 105K, corresponding to an astrophysical temperature of ~ 65 K (e.g. Boogert et al. 2000). The CO₂ evaporation temperature depends on the relative abundance of other species, particularly H₂O, but the mixtures with the most physically likely abundances (i.e. CO₂/H₂O < 1) have an average sublimation temperature of ~ 150 K, or 80K in astrophysical environments. Thus, the segregated column densities of Table 7 represent ices at circumstellar radii where the ice temperature is between 65 and 80K, and the “cold” + “warm” column densities indicate ice farther from the central source (i.e. where $T \lesssim 65$ K). The location of the “evaporation radius,” where the interstellar ice temperature exceeds ~ 80 K, determines the innermost boundary of the CO₂ ice mantles. The low-mass protostellar envelope models produced by Furlan et al. (2007) indicate these approximate temperature ranges in the densest inner regions ($R \lesssim 100$ AU); however, detailed physical structure models that also include the appropriate ice opacities are needed to further constrain the location and processing levels of the ices.

We show the dependence of thermal processing levels on the SED spectral index (indicative of the line-of-sight dust column) in Figure 15. The fraction of cold CO₂ ice increases (and the warm fraction decreases) for more deeply embedded objects, while the segregated fraction remains approximately constant. This suggests that once part of a protostellar environment has been warmed enough to segregate CO₂, the process becomes dominated by the rapid rate with which segregation and subsequent sublimation occur.

6.3. Comparison to ISM and Class 0 YSO Ices

We searched for a correlation between YSO evolutionary status and ice properties by extending our sample to include spectra of Taurus and Serpens cloud field stars—Elias 16 (Taurus; Bergin et al. 2005), Elias 13 and CK 2 (Taurus, Serpens; Knez et al. 2005), probing the cold molecular material in their respective clouds—as well as the Class 0 protostars CepE-MM (Cepheus) and L1448 IRS 2 (Perseus), observed and reduced in the same manner as our Class I/II sample (AOR IDs: 3623680, 3620352; Figure 16). We also included a spectrum of the line of sight towards the W3(OH) star formation region, which probes part of the foreground W3 molecular cloud (AOR ID 3566336).

For this secondary sample, we used the same procedures for continuum fitting and optical depth calculation as described in Section 3.1.1. CO₂ column densities were determined as in Section 5.4. Either noise or saturation of the absorption bands prevented detailed spectral fitting of the 6 μ m features, so we scaled a pure H₂O (10K) spectrum to match the peak optical depth at 6.0 μ m in order to calculate N(H₂O). The shape of the 6 μ m W3

spectrum is too irregular to be reasonably fit with a solid H₂O lab spectrum. For the other molecular cloud sight-lines, the N(H₂O) values were found to fall within 17% of published values (Table 8). The N(CO₂)/N(H₂O) ratios fell within at most 26% of the literature ratios, generally within less than 10%, when we use the customary band strength A of pure CO₂. For the Class 0 objects CepE-MM and L1448 IRS 2, we find N(CO₂)/N(H₂O) ratios of 0.09 and 0.1, respectively. These values are within the range consistently observed for many different sight-lines (Section 6.1), but when compared with our YSO sample, they are most closely consistent with the most deeply-embedded objects (as parameterized by α ; Figure 9). The cold cloud sight-lines have N(CO₂)/N(H₂O) of 0.14 (Elias 13), 0.2 (Elias 16), and 0.29 (CK 2). Thus while we appear to see a correlation between N(CO₂)/N(H₂O) and redness (thus evolutionary status) for the embedded objects, the interstellar values do not follow this trend. This deviation may be due to the fact that the ISM sight-lines probe a variety of environments and compositional structure from one edge of the cloud to the other, while protostellar sight-lines are dominated by the circumstellar material. Possibly interstellar regions of lower temperatures stifle CO₂ production mechanisms with activation barriers, as mentioned in Section 6.1, while areas of increased density favor H₂O production.

The 15.2 μ m feature in the molecular cloud sight-lines have previously been fitted with predominantly cold, polar H₂O:CO₂ mixtures (Bergin et al. 2005; Knez et al. 2005). We find that the χ^2_ν of the fits can be matched or reduced by including components containing methanol—specifically the cold counterpart of the H₂O:CH₃OH:CO₂ components used in our Class I/II fits (Figure 17). The percentage of polar ice found (\sim 75-80%) is comparable to that identified by Bergin et al. (2005) and Knez et al. (2005), and the abundance ratios N(CO₂)/N(H₂O) are preserved. All three interstellar cloud sight-lines show single-peaked 15.2 μ m profiles with very little substructure; CK 2 and Elias 16 are remarkably similar in shape, despite indications that ice mantles in Serpens may be fundamentally different from those in Taurus (Eiroa & Hodapp 1989). These results give support for the cold grain origin of at least some of the CH₃OH observed towards protostars; the presence of the unidentified 6.8 μ m band in background star sight-lines (particularly CK 2 and Elias 16; Knez et al. 2005) is consistent with the assignment of CH₃OH as a carrier.

Interestingly, the W3 spectrum, which has the reddest SED of our entire sample, shows a clear double-peaked CO₂ feature, indicating pure CO₂, which could have been formed by thermal segregation, along the line of sight (Figure 18). The segregation fraction is \sim 26%, comparable to the Class I/II average of \sim 30%. The most likely explanation is that this line of sight samples not only the cold foreground W3 cloud but also the warmer, thermally-processed CO₂ ices around the massive protostars in the W3(OH) region. The strong similarity of the 15.2 μ m absorption profile along this line of sight—which includes an ultra-compact HII region, strong outflows, and H₂O/OH maser emissions (Turner & Welch 1984; Alcolea et al. 1993; Argon et al. 2003)—to the profiles of the low-mass Taurus objects confirms the regularity and robustness of the solid CO₂ formation and evolution mechanisms. With higher angular resolution, observa-

tions of additional sight-lines in this rich region, including those towards the Class 0 object W3OH-TW, will provide useful information on the early stages of CO₂ heating in embedded objects.

Unfortunately, we could not fit either of the two Class 0 objects at 15.2 μ m—CepE-MM was observed at low resolution and L1448 IRS 2 has prohibitively large uncertainties in this wavelength range.

7. CONCLUSIONS

We have analyzed the mid-infrared molecular ice features in 16 Class I/II low-mass YSOs using Spitzer IRS observations. Using detailed comparisons to laboratory ice analog spectra, we find the ice mantle compositions to be dominated by H₂O and CO₂ ice but with significant abundances of additional species such as CH₃OH, H₂CO, HCOOH, NH₃, CH₄, and SO₂ (\lesssim 10% each).

Spectral fits to the 6 μ m feature reveal that \gtrsim 80% of the band can be attributed to H₂O, with additional absorptions near 5.85 μ m attributed to HCOOH and H₂CO. Some of the observed spectra have a broader 6 μ m peak that can be well-fit by H₂O:NH₃ ices, providing evidence for the presence of solid NH₃. On the long-wavelength wing of the 6 μ m feature, small absorption remnants are observed, varying in strength, shape, and peak position among the sources. We show these that are highly unlikely to be the result of PAH absorption, as has been proposed for massive YSOs (Schutte et al. 1996), due to the absence of other expected PAH features at 7.5-9 and 11-14 μ m.

We have examined the unidentified 6.8 μ m feature and discussed its assignment to solid CH₃OH and NH₄⁺, the two most common candidates. While no high-quality spectral fits could be achieved using these two components, we find that, on average, the observed YSO features could be approximately fit by equal contributions from NH₄⁺ and from a CH₃OH/H₂O \sim 0.1 mixture, with varying amounts of nearly-pure CH₃OH intermixed. However, we find a wide variety of feature shapes in our sample, indicating that the interstellar component(s) producing this band vary greatly from object to object, and a single simple carrier or set of carriers may be inadequate to explain the feature.

In the 7-8 μ m range, we are able to isolate and identify features attributed to CH₄, SO₂, and (tentatively) HCOOH ices. The high CH₄ ice abundances derived from these, along with the variety of feature shapes and peak positions within the sample, suggest variations in line-of-sight molecular environment or possible absorption contamination by unresolvable gas-phase CH₄ lines. The solid SO₂ and CH₄ band profiles are very sensitive to molecular environment and temperature, and additional high-resolution studies of this wavelength range will yield further information on molecular ice interactions and abundance structures along the line of sight.

The 15.2 μ m solid CO₂ bending mode feature is well-reproduced by multi-component laboratory fits comprising ice analogs (H₂O, CH₃OH, CO, CO₂) in various stages of radiative and thermal processing. Using the relative contribution of the components to each high-resolution feature profile, we find that all of the YSO ice environments have undergone at least some thermal heating, and 5 of the 9 have profiles entirely dominated by processed ices in which a significant fraction (\sim 20-

40%) of the CO₂ has segregated from the polar formation matrix.

The molecular ice abundance ratios, particularly N(CO₂)/N(H₂O), are consistent with the values observed in a wide variety of sight-lines, but within the sample, we observe a negative correlation between this ratio and the mid-infrared SED spectral index. This evidence describes a more complicated polar CO₂ environment than indicated by previous studies. Comparison of the SED spectral index with the ice temperatures derived from the 15.2 μm fits confirms the presence of cold ices in more deeply embedded objects and warmer, annealed ices in more evolved ones.

Comparison with molecular cloud sight-lines show that our fits are consistent with a scenario in which H₂O-rich grain mantles with CO₂ and CH₃OH relative abundances of ~20 and <10%, respectively, as well as traces of other species, form in the cold molecular clouds and are subsequently heated by young protostars. This thermal processing sublimates the most volatile species while induc-

ing molecular interactions and migrations that become spectroscopically detectable. The wide range of both molecular abundances and thermal processing levels observed within our sample indicates that young stars do have a strong effect on their surrounding environments.

We are grateful to Edwin Bergin and Claudia Knez for providing us with the field star spectra, to Melissa McClure for assistance with data reduction issues, and to Adwin Boogert for stimulating discussion. Extensive use was made of Leiden University's Sackler Laboratory ice analog databases and of the NASA ADS Abstract Service. This work is based on observations made with the Spitzer Space Telescope, which is operated by the Jet Propulsion Laboratory, California Institute of Technology under NASA contract 1407. Support for this work was provided by NASA through Contract Number 1257184 issued by JPL/Caltech. E.F. acknowledges support from a NASA Postdoctoral Program Fellowship.

REFERENCES

- Alcolea, J., Menten, K. M., Moran, J. M., & Reid, M. J. 1993, in *Lecture Notes in Physics*, Berlin Springer Verlag, Vol. 412, *Astrophysical Masers*, ed. A. W. Clegg & G. E. Nedoluha, 225–228
- Alexander, R. D., Casali, M. M., André, P., Persi, P., & Eiroa, C. 2003, *A&A*, 401, 613
- Allamandola, L. J., Sandford, S. A., & Valero, G. J. 1988, *Icarus*, 76, 225
- Andre, P., Ward-Thompson, D., & Barsony, M. 1993, *ApJ*, 406, 122
- Argon, A. L., Reid, M. J., & Menten, K. M. 2003, *ApJ*, 593, 925
- Bergin, E. A., Melnick, G. J., Gerakines, P. A., Neufeld, D. A., & Whittet, D. C. B. 2005, *ApJ*, 627, L33
- Bertout, C., Robichon, N., & Arenou, F. 1999, *A&A*, 352, 574
- Bisschop, S. E., Fuchs, G. W., Boogert, A. C. A., van Dishoeck, E. F., & Linnartz, H. 2007, *A&A*, 470, 749
- Boogert, A. C. A. & Ehrenfreund, P. 2004, in *Astronomical Society of the Pacific Conference Series*, Vol. 309, *Astrophysics of Dust*, ed. A. N. Witt, G. C. Clayton, & B. T. Draine, 547–+
- Boogert, A. C. A., Ehrenfreund, P., Gerakines, P. A., et al. 2000, *A&A*, 353, 349
- Boogert, A. C. A., Pontoppidan, K. M., Lahuis, F., et al. 2004, *ApJS*, 154, 359
- Boogert, A. C. A., Schutte, W. A., Helmich, F. P., Tielens, A. G. G. M., & Wooden, D. H. 1997, *A&A*, 317, 929
- Boogert, A. C. A., Schutte, W. A., Tielens, A. G. G. M., et al. 1996, *A&A*, 315, L377
- Bottinelli, S., Ceccarelli, C., Lefloch, B., et al. 2004, *ApJ*, 615, 354
- Cazaux, S., Tielens, A. G. G. M., Ceccarelli, C., et al. 2003, *ApJ*, 593, L51
- Chan, K. W., Roellig, T. L., Onaka, T., et al. 2000, in *ESA Special Publication*, Vol. 456, *ISO Beyond the Peaks: The 2nd ISO Workshop on Analytical Spectroscopy*, ed. A. Salama, M. F. Kessler, K. Leech, & B. Schulz, 59–+
- Chiar, J. E., Adamson, A. J., Kerr, T. H., & Whittet, D. C. B. 1995, *ApJ*, 455, 234
- Chiar, J. E., Ennico, K., Pendleton, Y. J., et al. 2007, *ApJ*, 666, L73
- Dartois, E., Demyk, K., d'Hendecourt, L., & Ehrenfreund, P. 1999, *A&A*, 351, 1066
- Ehrenfreund, P., Boogert, A. C. A., Gerakines, P. A., et al. 1996, *A&A*, 315, L341
- Ehrenfreund, P., Dartois, E., Demyk, K., & D'Hendecourt, L. 1998, *A&A*, 339, L17
- Ehrenfreund, P., Kerkhof, O., Schutte, W. A., et al. 1999, *A&A*, 350, 240
- Eiroa, C. & Hodapp, K.-W. 1989, *A&A*, 210, 345
- Forrest, W. J., Sargent, B., Furlan, E., et al. 2004, *ApJS*, 154, 443
- Furlan, E., Hartmann, L., Calvet, N., et al. 2006, *ApJS*, 165, 568
- Furlan, E., McClure, M., Calvet, N., et al. 2007, *ApJS*, in press (astro-ph/0711.4038)
- Gerakines, P. A., Schutte, W. A., & Ehrenfreund, P. 1996, *A&A*, 312, 289
- Gerakines, P. A., Schutte, W. A., Greenberg, J. M., & van Dishoeck, E. F. 1995, *A&A*, 296, 810
- Gerakines, P. A., Whittet, D. C. B., Ehrenfreund, P., et al. 1999, *ApJ*, 522, 357
- Gibb, E. L., Whittet, D. C. B., Boogert, A. C. A., & Tielens, A. G. G. M. 2004, *ApJS*, 151, 35
- Gibb, E. L., Whittet, D. C. B., Schutte, W. A., et al. 2000, *ApJ*, 536, 347
- Gillett, F. C., Jones, T. W., Merrill, K. M., & Stein, W. A. 1975, *A&A*, 45, 77
- Gomez, M., Hartmann, L., Kenyon, S. J., & Hewett, R. 1993, *AJ*, 105, 1927
- Grim, R. J. A., Baas, F., Greenberg, J. M., Geballe, T. R., & Schutte, W. 1991, *A&A*, 243, 473
- Grim, R. J. A., Greenberg, J. M., Schutte, W. A., & Schmitt, B. 1989, *ApJ*, 341, L87
- Hagen, W., Tielens, A. G. G. M., & Greenberg, J. M. 1981, *Chem. Phys.*, 56, 367
- Higdon, S. J. U., Devost, D., Higdon, J. L., et al. 2004, *PASP*, 116, 975
- Hony, S., Van Kerckhoven, C., Peeters, E., et al. 2001, *A&A*, 370, 1030
- Houck, J. R., Roellig, T. L., van Cleve, J., et al. 2004, *ApJS*, 154, 18
- Hudgins, D. M., Sandford, S. A., Allamandola, L. J., & Tielens, A. G. G. M. 1993, *ApJS*, 86, 713
- Keane, J. 1997, Master's thesis, Leiden University
- Keane, J. 2001, PhD thesis, Rijks Universiteit Groningen
- Keane, J. V. & Tielens, A. G. G. M. 2003, in *SFChem 2002: Chemistry as a Diagnostic of Star Formation*, proceedings of a conference held August 21–23, 2002 at University of Waterloo, Waterloo, Ontario, Canada N2L 3G1. Edited by Charles L. Curry and Michel Fich. NRC Press, Ottawa, Canada, 2003, p. 229., ed. C. L. Curry & M. Fich, 229–+
- Keane, J. V., Tielens, A. G. G. M., Boogert, A. C. A., Schutte, W. A., & Whittet, D. C. B. 2001, *A&A*, 376, 254
- Kenyon, S. J. & Hartmann, L. 1995, *ApJS*, 101, 117
- Khanna, R. K., Zhao, G., Ospina, M. J., & Pearl, J. C. 1988, *Spectrochimica Acta*, 44, 581
- Knez, C., Boogert, A. C. A., Pontoppidan, K. M., et al. 2005, *ApJ*, 635, L145
- Kouchi, A. & Kuroda, T. 1990, *Nature*, 344, 134
- Lacy, J. H., Faraji, H., Sandford, S. A., & Allamandola, L. J. 1998, *ApJ*, 501, L105+
- Lada, C. J. 1987, in *IAU Symposium*, Vol. 115, *Star Forming Regions*, ed. M. Peimbert & J. Jugaku, 1–17
- Maldoni, M. M., Smith, R. G., Robinson, G., & Rookyard, V. L. 1998, *MNRAS*, 298, 251
- Maréchal, Y. 1987, *J. Chem. Phys.*, 87, 6344

- Moore, M. H. & Hudson, R. L. 1992, *ApJ*, 401, 353
- Myers, P. C., Linke, R. A., & Benson, P. J. 1983, *ApJ*, 264, 517
- Nummelin, A., Whittet, D. C. B., Gibb, E. L., Gerakines, P. A., & Chiar, J. E. 2001, *ApJ*, 558, 185
- Öberg, K. I., Fraser, H. J., Boogert, A. C. A., et al. 2007, *A&A*, 462, 1187
- Palumbo, M. E. & Baratta, G. A. 2000, *A&A*, 361, 298
- Pontoppidan, K. M., Boogert, A. C. A., Fraser, H. J., et al. 2007, *ApJ*, in press (astro-ph/0711.4616)
- Pontoppidan, K. M., Dartois, E., van Dishoeck, E. F., Thi, W.-F., & d'Hendecourt, L. 2003, *A&A*, 404, L17
- Pontoppidan, K. M., Dullemond, C. P., van Dishoeck, E. F., et al. 2005, *ApJ*, 622, 463
- Puetter, R. C., Russell, R. W., Willner, S. P., & Soifer, B. T. 1979, *ApJ*, 228, 118
- Remijan, A., Shiao, Y.-S., Friedel, D. N., Meier, D. S., & Snyder, L. E. 2004, *ApJ*, 617, 384
- Rieke, G. H. & Lebofsky, M. J. 1985, *ApJ*, 288, 618
- Ruffle, D. P. & Herbst, E. 2001, *MNRAS*, 324, 1054
- Sandford, S. A. & Allamandola, L. J. 1990, *ApJ*, 355, 357
- Sandford, S. A. & Allamandola, L. J. 1993, *ApJ*, 417, 815
- Schutte, W. A., Allamandola, L. J., & Sandford, S. A. 1993, *Icarus*, 104, 118
- Schutte, W. A., Boogert, A. C. A., Tielens, A. G. G. M., et al. 1999, *A&A*, 343, 966
- Schutte, W. A. & Khanna, R. K. 2003, *A&A*, 398, 1049
- Schutte, W. A., Tielens, A. G. G. M., Whittet, D. C. B., et al. 1996, *A&A*, 315, L333
- Tielens, A. G. G. M. & Allamandola, L. J. 1987, in *Astrophysics and Space Science Library*, Vol. 134, *Interstellar Processes*, ed. D. J. Hollenbach & H. A. Thronson, Jr., 397–469
- Tielens, A. G. G. M. & Charnley, S. B. 1997, *Origins of Life and Evolution of the Biosphere*, 27, 23
- Tielens, A. G. G. M. & Hagen, W. 1982, *A&A*, 114, 245
- Tielens, A. G. G. M. & Whittet, D. C. B. 1996, in *IAU Symposium*, Vol. 178, *Molecules in Astrophysics: Probes & Processes*, ed. E. F. van Dishoeck, 45–+
- Turner, J. L. & Welch, W. J. 1984, *ApJ*, 287, L81
- van Broekhuizen, F. A., Groot, I. M. N., Fraser, H. J., van Dishoeck, E. F., & Schlemmer, S. 2006, *A&A*, 451, 723
- van Dishoeck, E. F. 2003, in *SFChem 2002: Chemistry as a Diagnostic of Star Formation*, proceedings of a conference held August 21-23, 2002 at University of Waterloo, Waterloo, Ontario, Canada N2L 3G1. Edited by Charles L. Curry and Michel Fich. NRC Press, Ottawa, Canada, 2003, p. 201., ed. C. L. Curry & M. Fich, 201–+
- van Dishoeck, E. F. 2006, *Proceedings of the National Academy of Science*, 103, 12249
- van Dishoeck, E. F. & Blake, G. A. 1998, *ARA&A*, 36, 317
- van Dishoeck, E. F., Helmich, F. P., de Graauw, T., et al. 1996, *A&A*, 315, L349
- Watson, D. M., Kemper, F., Calvet, N., et al. 2004, *ApJS*, 154, 391
- Werner, M. W., Roellig, T. L., Low, F. J., et al. 2004, *ApJS*, 154, 1
- White, R. J. & Ghez, A. M. 2001, *ApJ*, 556, 265
- Whittet, D. C. B., Bode, M. F., Longmore, A. J., et al. 1988, *MNRAS*, 233, 321
- Whittet, D. C. B., Boogert, A. C. A., Gerakines, P. A., et al. 1997, *ApJ*, 490, 729
- Whittet, D. C. B., Shenoy, S. S., Bergin, E. A., et al. 2007, *ApJ*, 655, 332
- Willner, S. P., Gillett, F. C., Herter, T. L., et al. 1982, *ApJ*, 253, 174

TABLE 1

OVERVIEW OF THE SPITZER IRS OBSERVATIONS OF OUR SAMPLE OF CLASS I/II SOURCES. THE FIRST COLUMN GIVES THE SOURCE NAME, AND THE SECOND TO FOURTH COLUMNS GIVE THE OBSERVATIONS' AOR KEY, DATE, AND IRS MODULES/MODE USED (SL: SHORT-LOW, SH: SHORT-HIGH, LL: LONG-LOW, LH: LONG-HIGH).

Object	AOR	Obs. Date (2004)	IRS Modules/Mode
IRAS 04016+2610	3528960	2/07	SL,SH,LH Map
IRAS 04108+2803A	3539712	2/06	SL,LL Stare
IRAS 04108+2803B	3529472	2/06	SL,SH,LH Map
IRAS 04154+2823	3534336	3/03	SL,LL Map
IRAS 04169+2702	3534848	3/04	SL,LL Map
IRAS 04181+2654A	3546112	2/29	SL,LL Stare
IRAS 04181+2654B	3545856	2/07	SL,LL Stare
IRAS 04239+2436	3530752	2/08	SL,SH,LH Map
IRAS 04295+2251	3537408	2/27	SL,LL Map
IRAS 04361+2547	3533056	2/29	SL,SH,LH Map
IRAS 04365+2535	3533312	2/27	SL,SH,LH Map
IRAS 04381+2540	3538944	2/27	SL,LL Map
DG Tau B	3540992	2/08	SL,SH,LH Stare
HL Tau	3531776	3/04	SL,SH,LH Map
IC 2087 IR	3533312	2/27	SL,SH,LH Map
L1551 IRS 5	3531776	3/04	SL,SH,LH Map

TABLE 2
 ABSORPTION FEATURES IDENTIFIED IN OUR YSO SPECTRA.

Wavelength (μm)	Carrier(s)	Mode	A ($10^{-17}\text{cm molec}^{-1}$)	Reference
Ice Features				
5.81	H ₂ CO	C=O stretching	0.96	1
5.85	HCOOH	C=O stretching	6.7	2
6.0	H ₂ O	H-O-H bending	1.2-1.3 ^a	3
6.8	CH ₃ OH?, NH ₄ ⁺ ?, organics	O-H bending, C-H deforming	...	
7.58	SO ₂	S-O stretching	3.4	4
7.7	CH ₄	C-H deforming	0.73	4
15.2	CO ₂	O-C-O bending	1.5 ^b	3
Other Features				
9.7	Silicates	Si-O stretching	...	
14.97	CO ₂	gas-phase ν_2 bend	...	5
18-20	Silicates	O-Si-O bending	...	

REFERENCES. — (1) Schutte et al. (1993), (2) Maréchal (1987), (3) Gerakines et al. (1995), (4) Boogert et al. (1997), (5) van Dishoeck et al. (1996)

^a A depends on temperature; range represents 10-120K^b A for H₂O:CO₂ mix, see Section 3.3

TABLE 3
 CHARACTERISTICS OF OUR SAMPLE OF TAURUS CLASS I/II
 OBJECTS. THE FIRST COLUMN GIVES THE OBJECT NAME, THE
 SECOND AND THIRD COLUMNS GIVE THE 6.0 μM AND 15.2 μM
 PEAK OPTICAL DEPTHS, AND THE FOURTH COLUMN GIVES THE
 SED SPECTRAL INDEX α (14.5-30 μm ; EQUATION 3).

Object	$\tau_{6.0\mu\text{m}}$	$\tau_{15.2\mu\text{m}}$	SED α
IRAS 04016+2610	0.38(± 0.01)	0.73(± 0.01)	0.64(± 0.07)
IRAS 04108+2803A	0.19(± 0.01)	0.19(± 0.01)	0.57(± 0.21)
IRAS 04108+2803B	0.26(± 0.01)	0.43(± 0.01)	0.58(± 0.23)
IRAS 04154+2823	0.08(± 0.01)	0.16(± 0.01)	-0.03(± 0.07)
IRAS 04169+2702	0.25(± 0.01)	0.31(± 0.01)	1.22(± 0.05)
IRAS 04181+2654A	0.2(± 0.01)	0.3(± 0.01)	0.13(± 0.05)
IRAS 04181+2654B	0.32(± 0.03)	0.44(± 0.01)	0.92(± 0.06)
IRAS 04239+2436	0.25(± 0.01)	0.44(± 0.01)	0.62(± 0.35)
IRAS 04295+2251	0.2(± 0.02)	0.18(± 0.01)	0.30(± 0.04)
IRAS 04361+2547	0.45(± 0.01)	0.27(± 0.03)	1.80(± 0.08)
IRAS 04365+2535	0.33(± 0.01)	0.63(± 0.01)	1.11(± 0.08)
IRAS 04381+2540	0.44(± 0.01)	0.62(± 0.01)	1.16(± 0.02)
DG Tau B	0.34(± 0.04)	0.3(± 0.01)	0.38(± 0.3)
HL Tau	0.12(± 0.01)	0.12(± 0.01)	0.75(± 0.07)
IC 2087 IR	0.14(± 0.01)	0.33(± 0.01)	-0.71(± 0.03)
L1551 IRS 5	0.54(± 0.01)	0.58(± 0.03)	1.62(± 0.11)

TABLE 4
LABORATORY SPECTRA USED IN 6 μM FITS.

Composition	Temperature (K)	Radiation ^a
Pure H ₂ O	10	...
Pure H ₂ O	30	...
Pure H ₂ O	50	...
Pure H ₂ O	120	...
Pure H ₂ CO	10	...
Pure HCOOH	10	...
H ₂ O:CH ₄ ^b 1:0.33	50	1 hr
H ₂ O:NH ₃ 1:0.2	10	1 hr

REFERENCES. — All spectra from Leiden University's Sackler Laboratory ice analog databases.

^a The equivalent of $10^{15} \text{cm}^{-2} \text{s}^{-1}$ photons ($E_\gamma > 6 \text{eV}$) for the noted length of time ^b CH₄ does not have a resonance at 6 μm but its presence in a water ice matrix affects the shape of the feature.

TABLE 5
 DERIVED SOLID-STATE MOLECULAR ABUNDANCES IN OUR YSO SAMPLE. THE
 FIRST COLUMN GIVES THE OBJECT NAME, AND THE SECOND THROUGH EIGHTH
 COLUMNS GIVE THE COLUMN DENSITIES OF H₂O, CO₂, H₂CO, HCOOH, NH₃,
 SO₂, CH₄, AND CH₃OH.

Object	N(H ₂ O) 10 ¹⁸ cm ⁻²	N(CO ₂) ^a 10 ¹⁷ cm ⁻²	N(H ₂ CO) ^b 10 ¹⁶ cm ⁻²	N(HCOOH) ^{b,c} 10 ¹⁶ cm ⁻²	N(NH ₃) 10 ¹⁷ cm ⁻²	N(SO ₂) 10 ¹⁶ cm ⁻²	N(CH ₄) 10 ¹⁷ cm ⁻²	N(CH ₃ OH) ^e 10 ¹⁷ cm ⁻²
IRAS 04016+2610	5.91 ±0.2	10.20 ±1.4	11.30	10.80	<7.16	<0.52	0.23 ±0.2	9.2
IRAS 04108+2803A	2.90 ±0.3	2.74 ±0.5	0.84	1.80	<2.61	4.92 ±2.8	2.33 ±0.5	9.2
IRAS 04108+2803B	4.44 ±0.2	4.95 ±0.8	9.59	3.37	<4.00	<3.18 ^d	2.50 ±0.4	4.4
IRAS 04154+2823	1.07 ±0.2	2.00 ±0.4	0.14	0.03	<3.04	<0.52	2.48 ±0.4	1.8
IRAS 04169+2702	4.33 ±0.2	4.33 ±0.7	10.40	4.21	<3.89	<0.52 ^d	1.68 ±0.4	7.3
IRAS 04181+2654A	3.63 ±0.2	4.09 ±0.6	13.10	0.58	<3.27	<0.52 ^d	1.14 ±0.4	3.3
IRAS 04181+2654B	4.18 ±0.4	6.42 ±0.9	29.60	2.80	<10.70	<1.27	1.90 ±0.7	11.8
IRAS 04239+2436	4.44 ±0.2	5.60 ±0.8	10.80	0.00	<5.55	2.75 ±0.8	<0.23	3.9
IRAS 04295+2251	2.82 ±0.3	2.65 ±0.5	4.69	1.25	<4.31	<2.75 ^d	0.67 ±0.4	4.4
IRAS 04361+2547	7.38 ±0.3	3.64 ±1.0	0.00	6.91	<6.64	<0.73	3.14 ±0.4	10.4
IRAS 04365+2535	5.31 ±0.2	8.01 ±1.2	9.69	2.63	<6.89	<0.52	0.40 ±0.3	3.3
IRAS 04381+2540	7.92 ±0.2	9.27 ±1.3	6.62	3.91	<7.28	1.50 ±0.6	0.27 ±0.2	6.3
DG Tau B	5.65 ±0.6	4.24 ±0.7	0.00	2.76	<10.00	6.87 ±2.5	<0.23	9.7
HL Tau	1.91 ±0.2	1.40 ±0.4	11.20	1.25	<2.11	1.97 ±0.8	<0.23	2.0
IC 2087 IR	2.13 ±0.2	4.12 ±0.7	1.70	0.14	<5.68	<0.52	0.39 ±0.4	2.7
L1551 IRS 5	10.90 ±0.2	8.65 ±1.7	0.14	0.03	<9.82	<0.52	1.86 ±0.4	8.8

^a Using band strength of H₂O:CO₂ mixture; see Section 6.1. ^b N(H₂CO) and N(HCOOH) have typical uncertainties of ~10%. ^c Based on 5.8 μm feature alone. ^d A feature was detected in the SO₂ wavelength range but with an overly-narrow width; value given is an upper limit. ^e Estimated from 6.8 μm feature; typical uncertainty is 2×10¹⁷cm⁻².

TABLE 6
LABORATORY SPECTRA USED IN 15 μm FITS.

Composition	Temperature (K)	Radiation ^a	Reference
H ₂ O:CH ₃ OH:CO ₂ 0.9:0.3:1	98	...	1
H ₂ O:CH ₃ OH:CO ₂ 1:1:1	130	...	1
CO:H ₂ O 10:1	30	1 hr	2
H ₂ O:CO ₂ 10:1	10	...	3
Pure CO ₂	10	...	3

REFERENCES. — (1) Ehrenfreund et al. (1999), (2) Gerakines et al. (1995), (3) Ehrenfreund et al. (1996)

^a The equivalent of $10^{15}\text{cm}^{-2}\text{s}^{-1}$ photons ($E_{\gamma} > 6\text{ eV}$) for the noted length of time

TABLE 7
 PERCENTAGE AND COLUMN DENSITY N (10^{17}cm^{-2}) OF CO_2 ICE PRESENT IN
 EACH STAGE OF PROCESSING ALONG THE LINE OF SIGHT: COLD, WARM, AND
 SEGREGATED.

Object	Cold		Warm		Segregated	
	% Total	N	% Total	N	% Total	N
IRAS 04016+2610	3	0.28	71	7.3	26	2.6
IRAS 04108+2803B	33	1.6	30	1.5	37	1.8
IRAS 04239+2436	10	0.57	87	4.9	2	0.14
IRAS 04361+2547	62	2.2	12	0.45	26	0.95
IRAS 04365+2535	2	0.17	61	4.9	37	2.9
DG Tau B	1	0.05	76	3.2	23	1.0
HL Tau	32	0.45	32	0.44	36	0.51
IC 2087 IR	9	0.35	68	2.8	23	0.95
L1551 IRS 5	22	1.9	54	4.6	24	2.1

NOTE. — Due to rounding, percentages may not sum to exactly 100%.

TABLE 8
MOLECULAR CLOUD ABUNDANCES.

Source	$N(\text{H}_2\text{O})$ (10^{18}cm^{-2}) [This work]	$N(\text{H}_2\text{O})$ (10^{18}cm^{-2}) [Lit., (Refs)]	$N(\text{CO}_2)/N(\text{H}_2\text{O})^a$ [This work]	$N(\text{CO}_2)/N(\text{H}_2\text{O})$ [Lit., (Refs)]
CK 2	2.9	3.5 (1)	0.29	0.33 (2)
Elias 13	0.95	1.0 (3)	0.14	0.15,0.19 (2,5)
Elias 16	2.2	2.5 (4)	0.2	0.18,0.23 (3,5)

REFERENCES. — (1) Eiroa & Hodapp (1989), (2) Knez et al. (2005), (3) Whittet et al. (1988), (4) Chiar et al. (1995), (5) Nummelin et al. (2001)

^a $N(\text{CO}_2)$ calculated using the band strength A of pure CO_2 in order to facilitate comparison with published values.

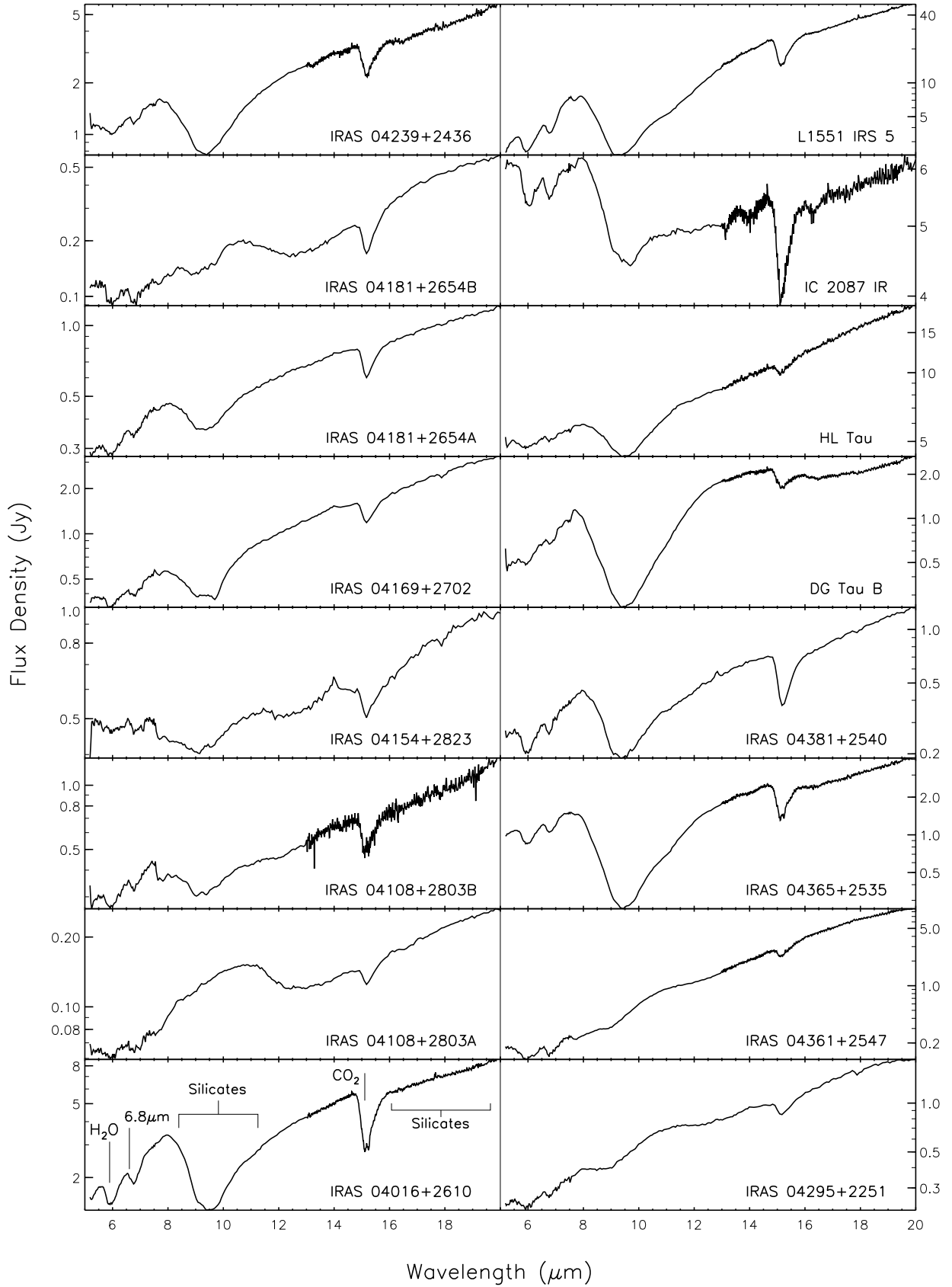


FIG. 1.— Our sample IRS spectra. The lower left object has been marked with the locations and primary carriers of the most prominent absorption features. Note that occasionally the silicate feature appears partly or wholly in emission.

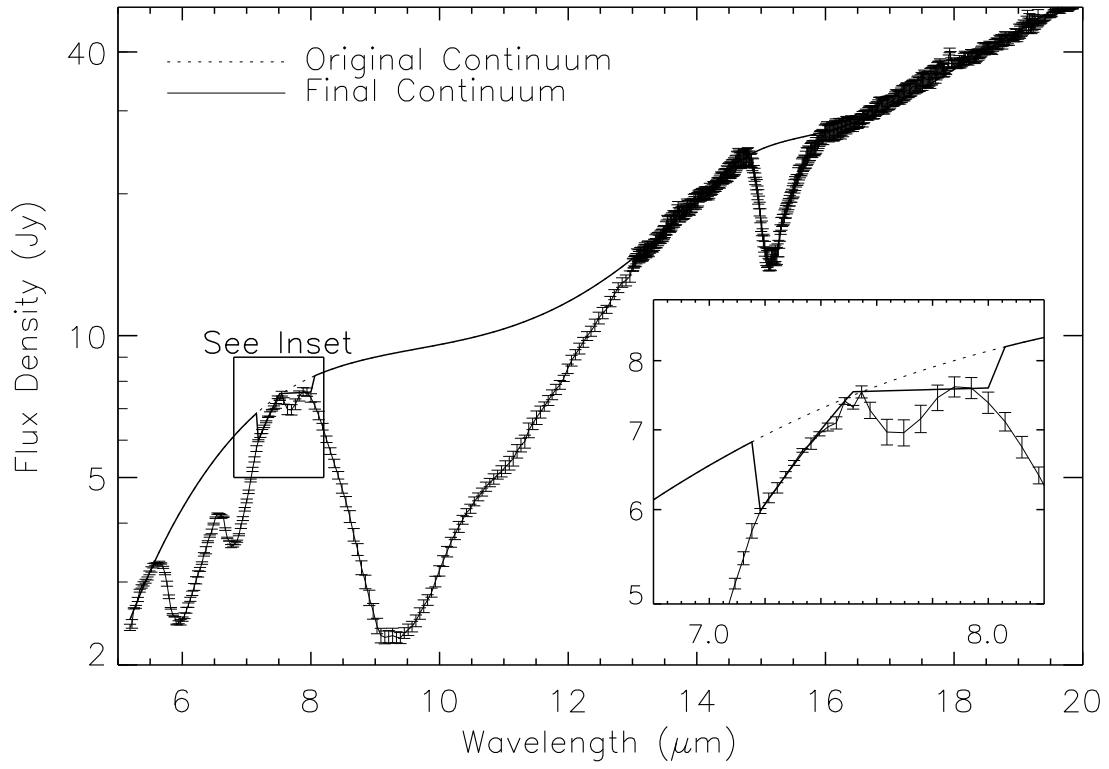


FIG. 2.— Example of the applied continuum determination using the spectrum of L1551 IRS 5. The inset shows the additional continuum imposed on the 7-8 μm range.

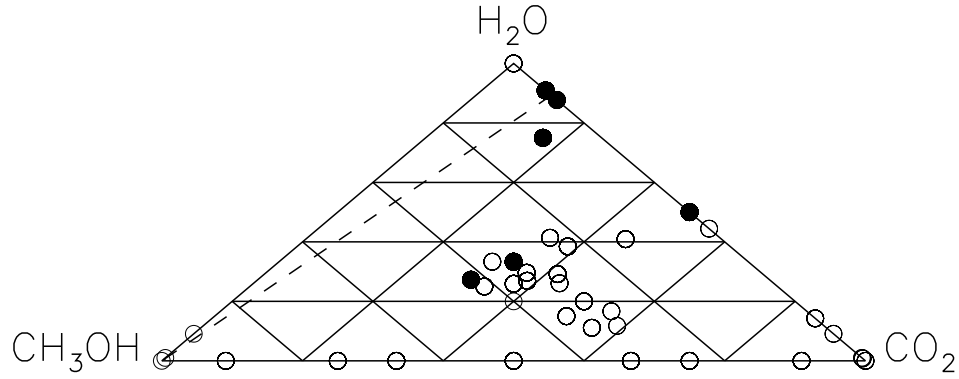


FIG. 3.— Range of non-irradiated H₂O:CH₃OH:CO₂ laboratory compositions for which there is infrared spectroscopy in the Leiden University database. The vertices represent the pure molecular ices, and distance from each molecule's vertex indicates decreasing relative abundance of that molecule (the lines are at increments of 20%). The filled circles represent mixtures whose $\tau_{6.0}/\tau_{15.2}$ ratio falls within the range spanned by the ratios from the YSO spectra (Section 4), and the dashed line indicates compositions wherein $\text{CO}_2/\text{H}_2\text{O}=0.12$ (Section 6.1).

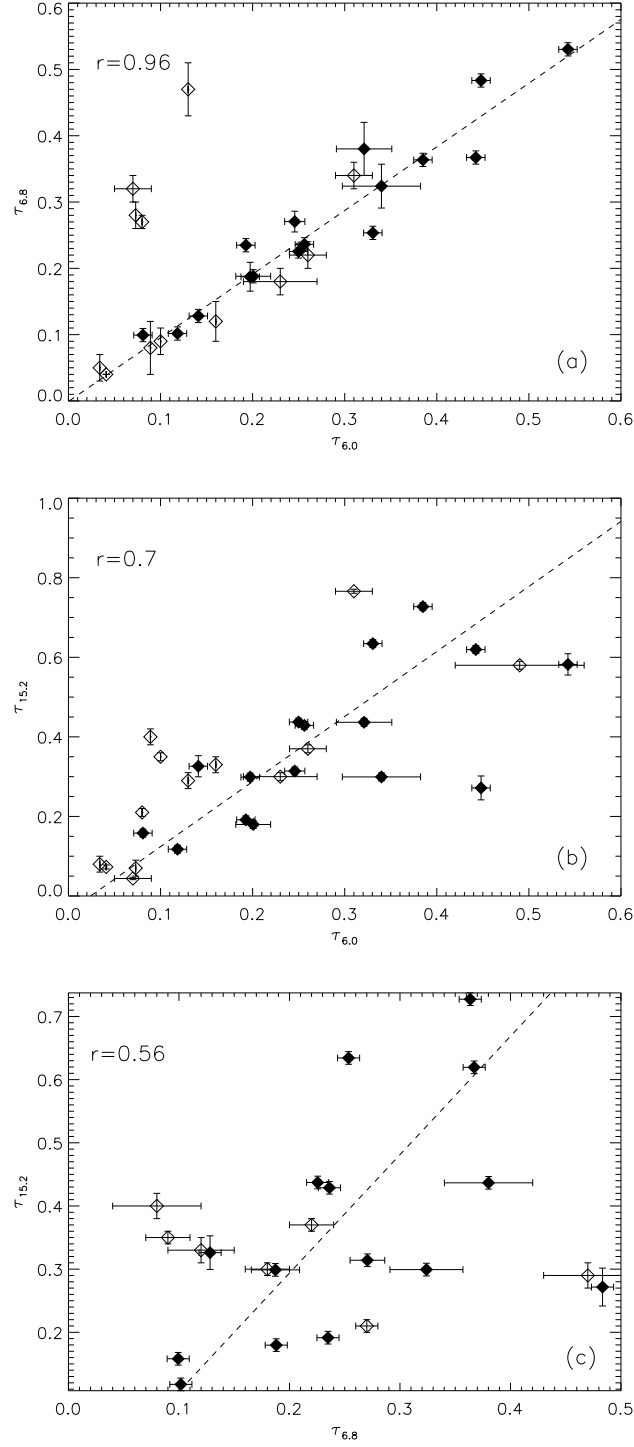


FIG. 4.— Relationships between feature peak optical depths for our low-mass YSOs (filled diamonds) and high-mass YSOs from Gibb et al. (2004) (open diamonds). Panel (a) shows $\tau_{6.8\mu\text{m}}$ vs $\tau_{6.0\mu\text{m}}$, panel (b) shows $\tau_{15.2\mu\text{m}}$ vs $\tau_{6.0\mu\text{m}}$, and panel (c) shows $\tau_{15.2\mu\text{m}}$ vs $\tau_{6.8\mu\text{m}}$. The dashed lines indicate the best linear fit to our data points.

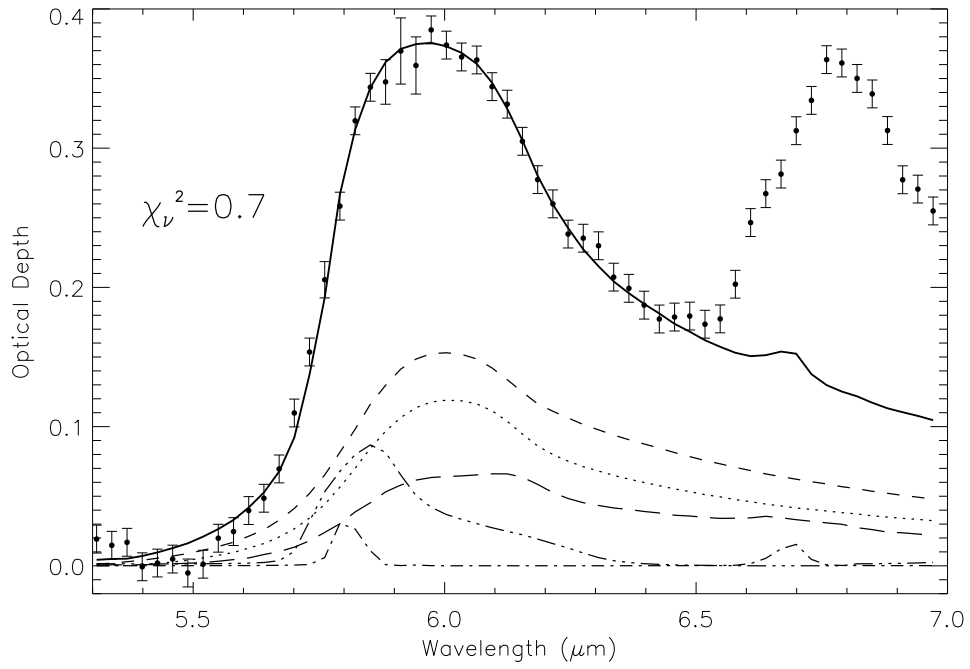


FIG. 5.— The $6\ \mu\text{m}$ feature of IRAS 04016+2610, fit by a combination of pure H_2O at 10 and 50K (dots/short dashes), pure H_2CO at 10K (dot-dash), pure HCOOH at 10K (dash-triple dots), and $\text{H}_2\text{O}:\text{NH}_3$ 1:0.2 at 10K (long dashes). The solid line is the sum. The $6.8\ \mu\text{m}$ feature is deliberately excluded from the fit.

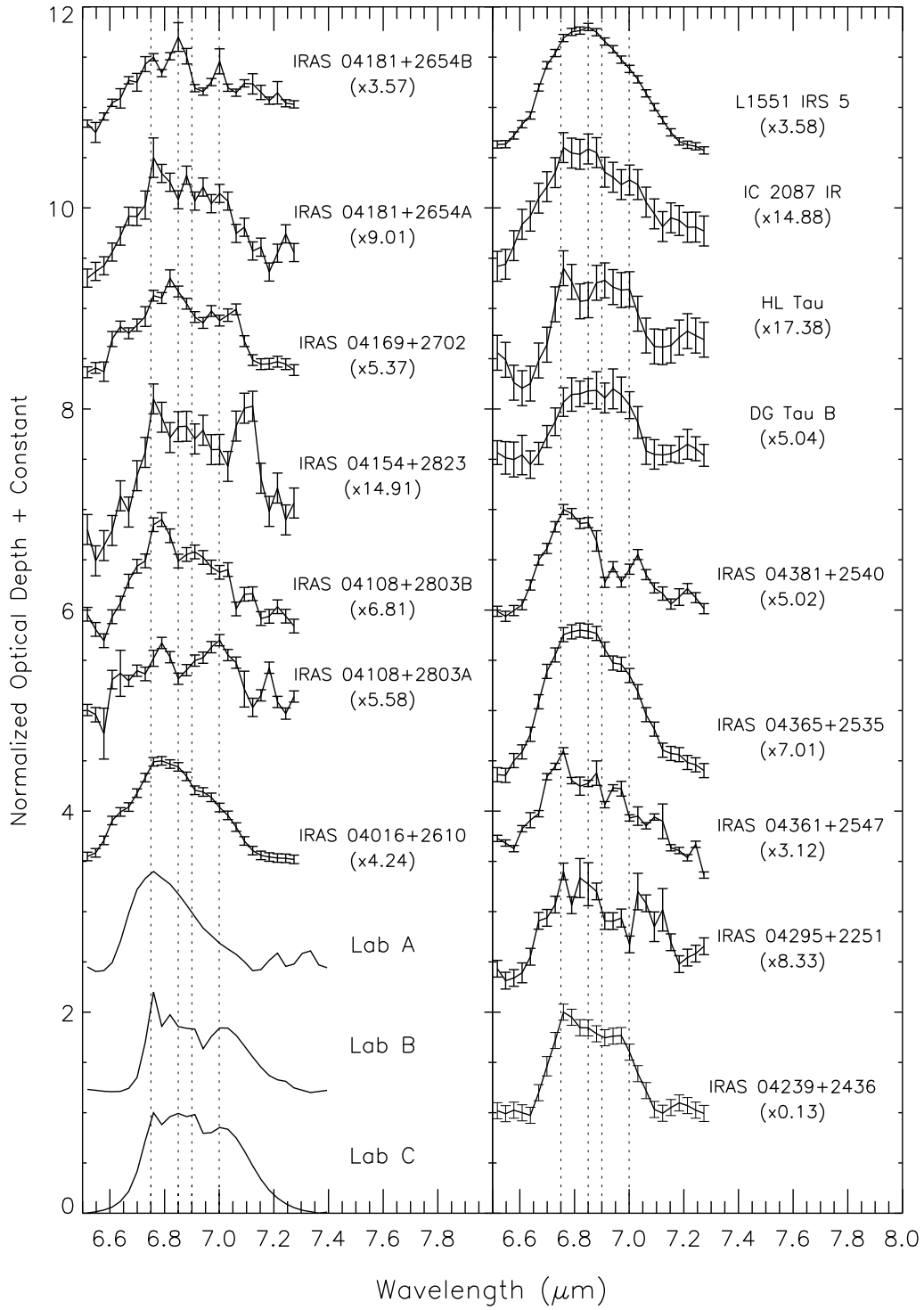


FIG. 6.— Our sample's $6.8 \mu\text{m}$ profiles (after subtraction of the $6 \mu\text{m}$ feature contributions) normalized to 1 and shifted vertically. Also shown for comparison are normalized laboratory spectra—A: $\text{H}_2\text{O}:\text{CO}:\text{NH}_3$ 10:2.5:2 at 165K (irradiated to create NH_4^+), B: $\text{H}_2\text{O}:\text{CH}_3\text{OH}:\text{CO}_2$ 9:1:2 at 10K, C: $\text{H}_2\text{O}:\text{CH}_3\text{OH}$ 1:100 at 10K. The dotted lines indicate the subpeak positions of the CH_3OH mixtures.

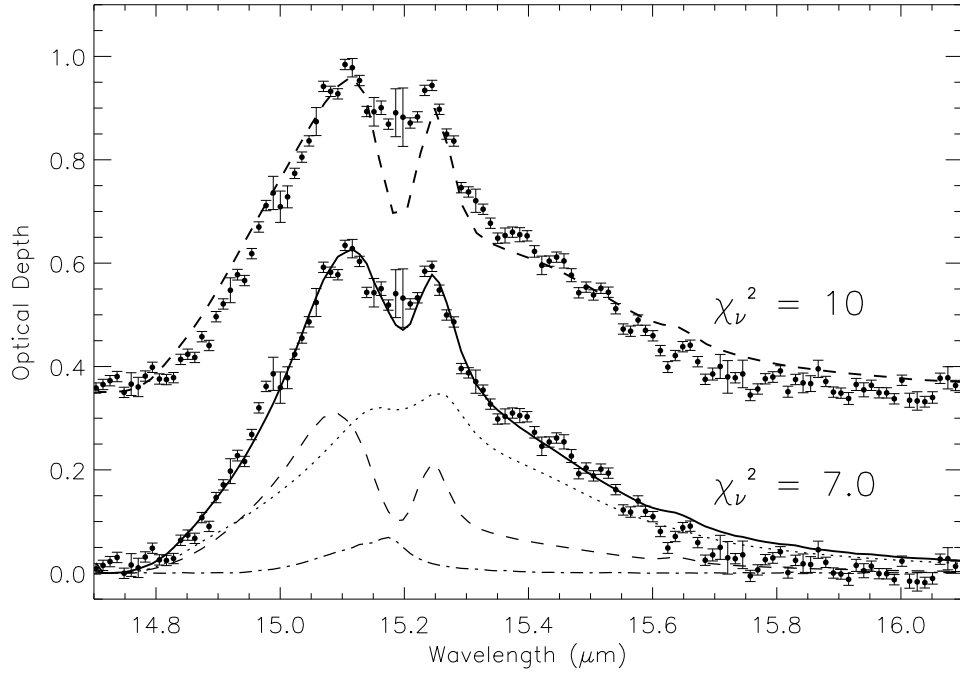


FIG. 7.— $15\ \mu\text{m}$ feature of IRAS 04365+2535, shown repeated with a vertical offset (0.35). The spectrum on the bottom is overlaid with a fit of $\text{H}_2\text{O}:\text{CH}_3\text{OH}:\text{CO}_2$ 0.9:0.3:1 at 98K (dots), $\text{H}_2\text{O}:\text{CH}_3\text{OH}:\text{CO}_2$ 1:1:1 at 130K (dashes), and $\text{CO}:\text{H}_2\text{O}$ 10:1 at 30K (dash-dot). The solid line is the sum. The heavy dashed fit on the upper spectrum is a fit using only $\text{H}_2\text{O}:\text{CH}_3\text{OH}:\text{CO}_2$ 1:1:1 at 118K. The excess between 14.95 and $15\ \mu\text{m}$ is due to the gas-phase CO_2 ro-vibrational ν_2 Q-branch lines, blended together at this resolution.

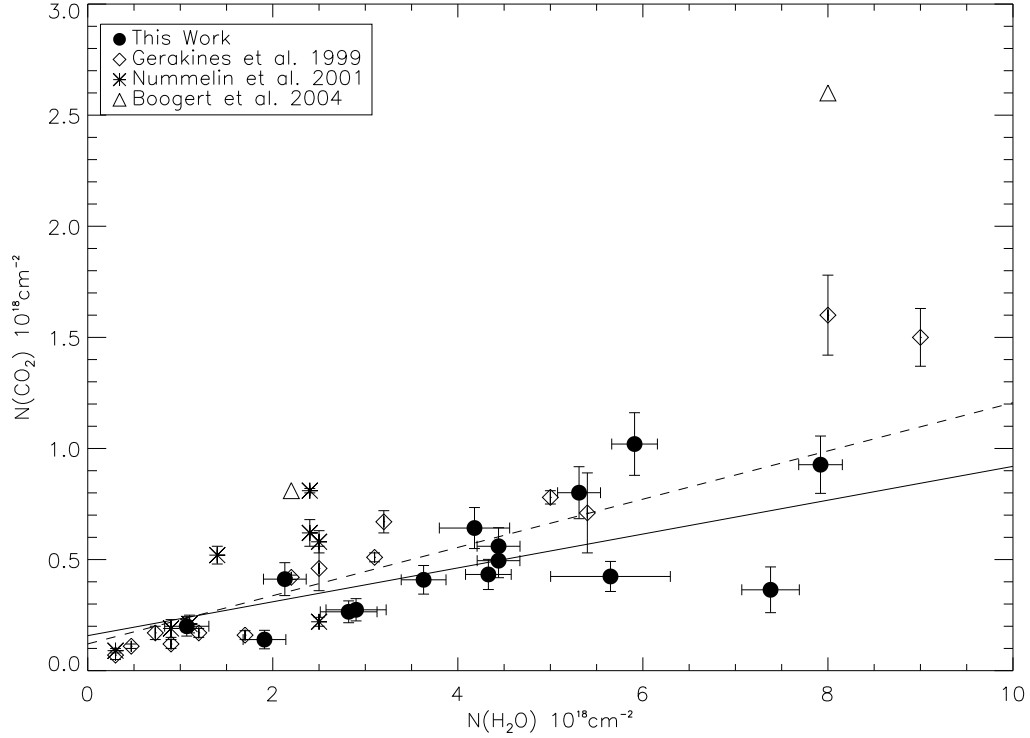


FIG. 8.— Correlation between solid $N(\text{H}_2\text{O})$ and $N(\text{CO}_2)$ for many different lines of sight. Our sample comprises low-mass protostars, Gerakines et al. (1999) contains mostly massive protostars and some galactic center sources, Nummelin et al. (2001) comprises low- and high-mass YSOs as well as some molecular cloud sight-lines, and Boogert et al. (2004) contains two low-mass protostars. The solid line is the ratio between column densities using only the current work's sample, and the dashed line is the ratio using all objects except the upper outlier from Boogert et al. (2004). Note that this work uses a CO_2 band strength $\sim 36\%$ higher than that of the previous studies, which accounts for most of the difference in $N(\text{CO}_2)$.

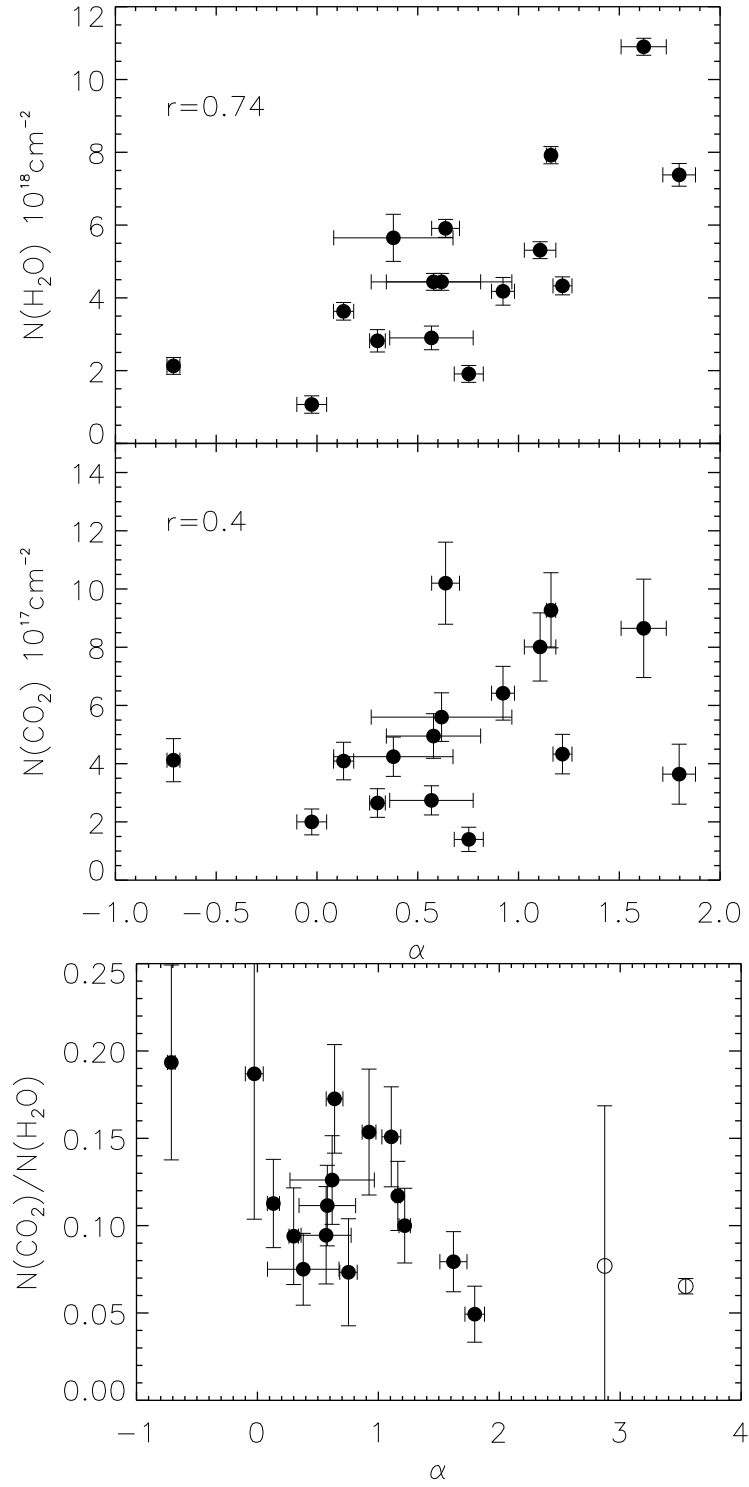


FIG. 9.— Correlations between the SED spectral index (α ; 14.5-30 μm) and $N(\text{CO}_2)$, $N(\text{H}_2\text{O})$, and $N(\text{CO}_2)/N(\text{H}_2\text{O})$. The filled circles represent our Class I/II data, and the open circles represent the Class 0 objects (Section 6.3).

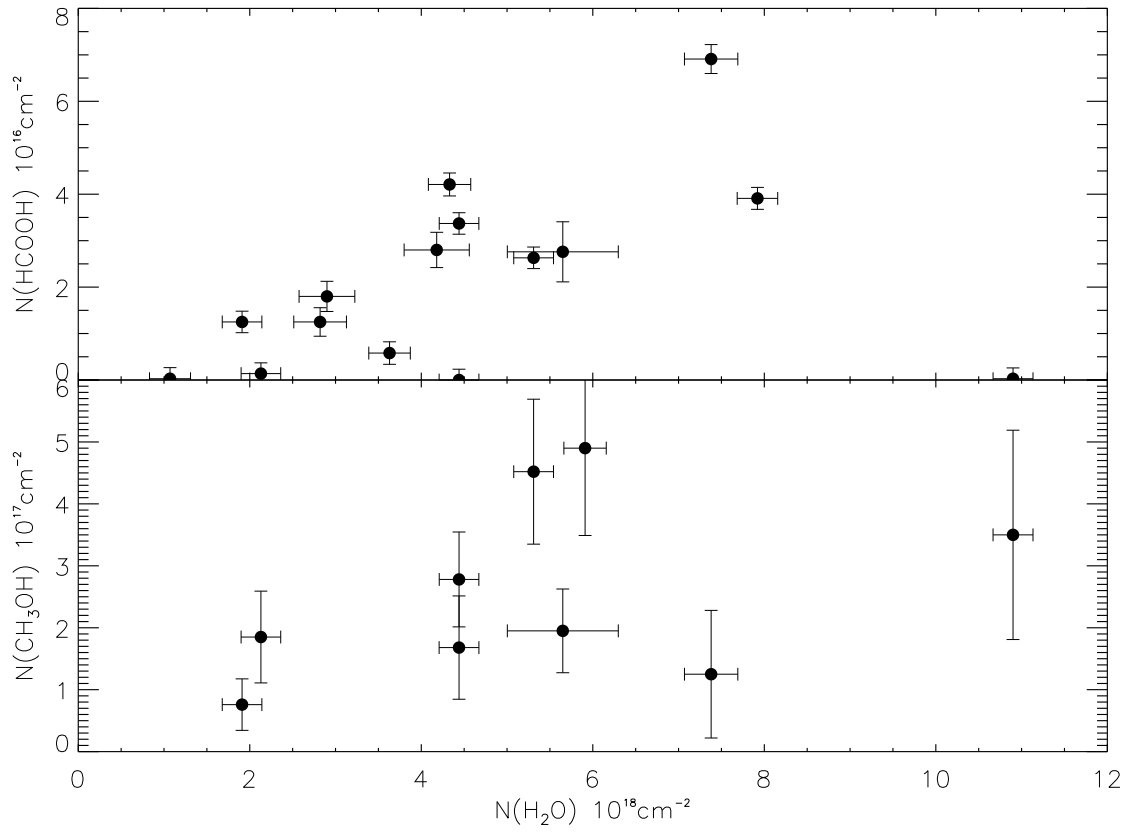


FIG. 10.— Ratios between $N(\text{H}_2\text{O})$, and $N(\text{HCOOH})$ and $N(\text{CH}_3\text{OH})$, for the Class I/II sample (Section 6.1). The bottom plot refers to $N(\text{CH}_3\text{OH})$ embedded in a $\text{H}_2\text{O}:\text{CO}_2$ matrix.

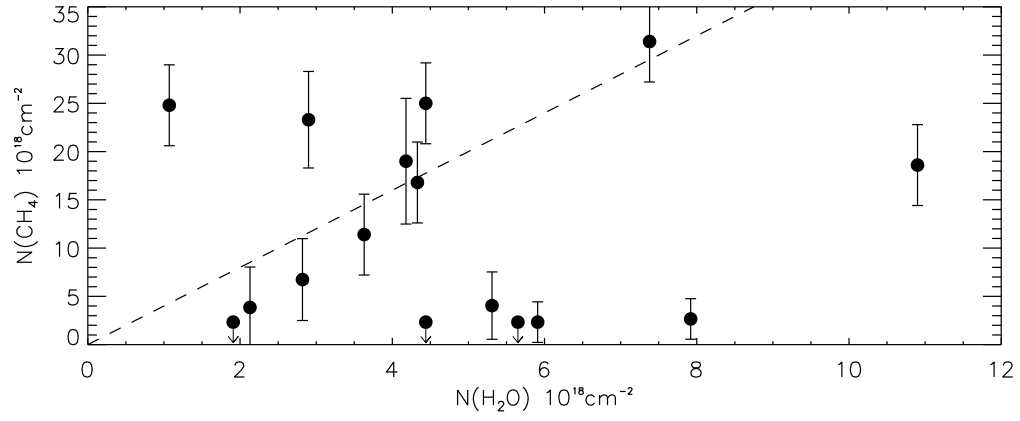


FIG. 11.— Comparison of solid $N(\text{H}_2\text{O})$ and $N(\text{CH}_4)$ for the YSO sample. The dashed line indicates the maximum of $\sim 4\%$ (CH_4 relative to H_2O) observed towards massive protostars (e.g. Gibb et al. 2004).

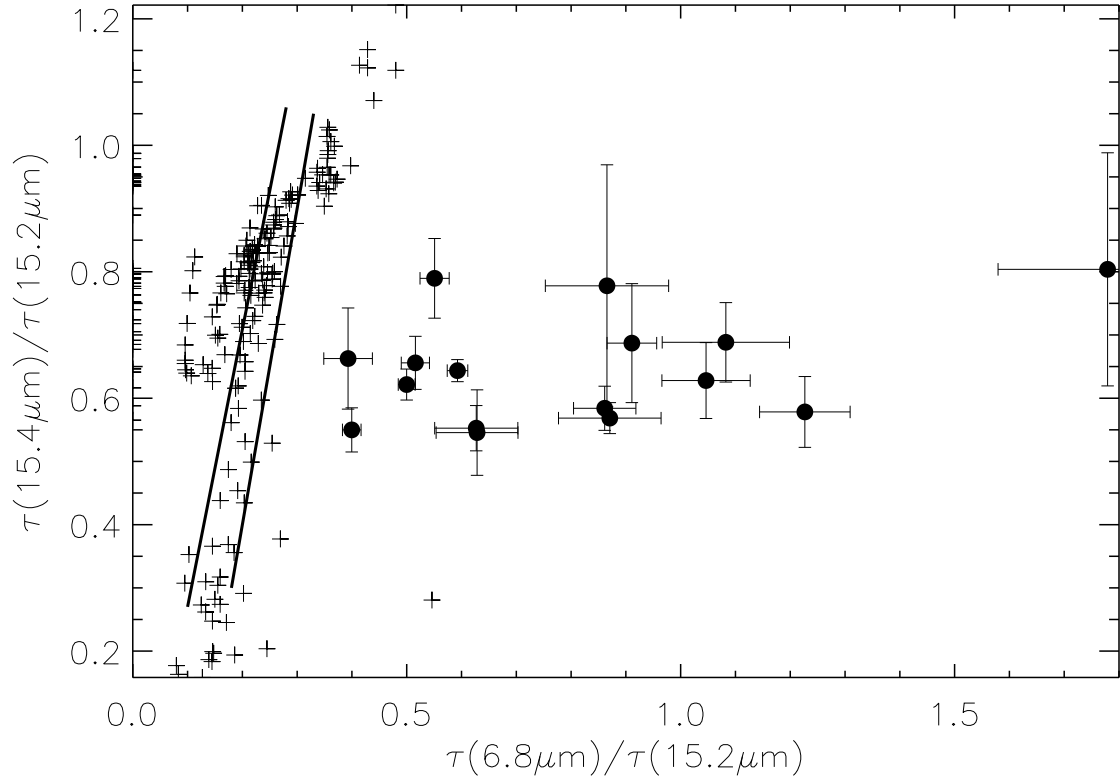


FIG. 12.— The correlation between 6.8 μm and 15.4 μm optical depths in the laboratory ice spectra (plus signs) and the observed YSO spectra (solid circles). Both have been scaled by peak 15.2 μm optical depth. The laboratory data cover temperatures from 10-185K and $\text{CH}_3\text{OH}/\text{CO}_2$ abundance ratios of 0-1.4, which are roughly indicated by the solid lines: $\lesssim 0.5$ / $0.5-1.4$ / $\gtrsim 1.4$. The vertical spread depends largely on temperature, with warmer mixtures of a constant composition showing weaker 15.4 μm shoulders.

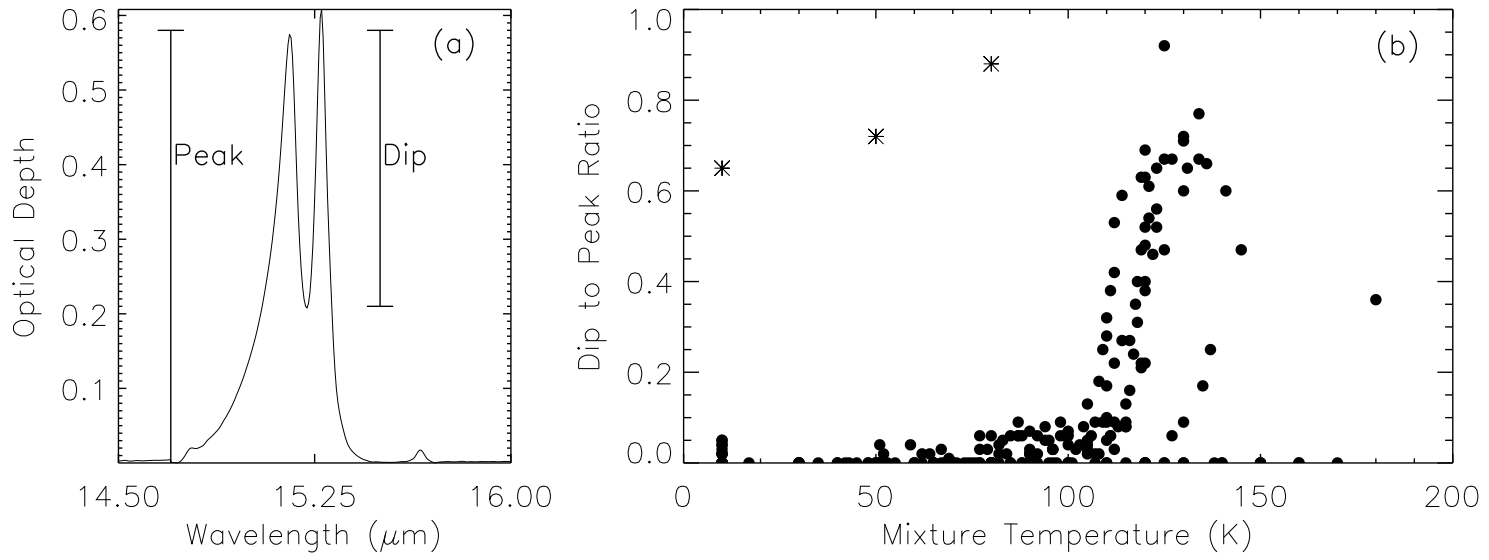


FIG. 13.— The “dip”-to-“peak” ratio as a measure of the amount of CO_2 segregation. (a)—Demonstrates how the values were measured for each laboratory ice spectrum, using pure CO_2 as an example. (b)—The relative dip strength as a function of laboratory ice temperature, showing the rapid onset of the process near $\sim 105\text{K}$. Much of the scatter in (b) is due to the dependence of CO_2 segregation temperature on the exact composition of the matrix in which it is embedded. The large asterisks in the upper left represent pure CO_2 ice.

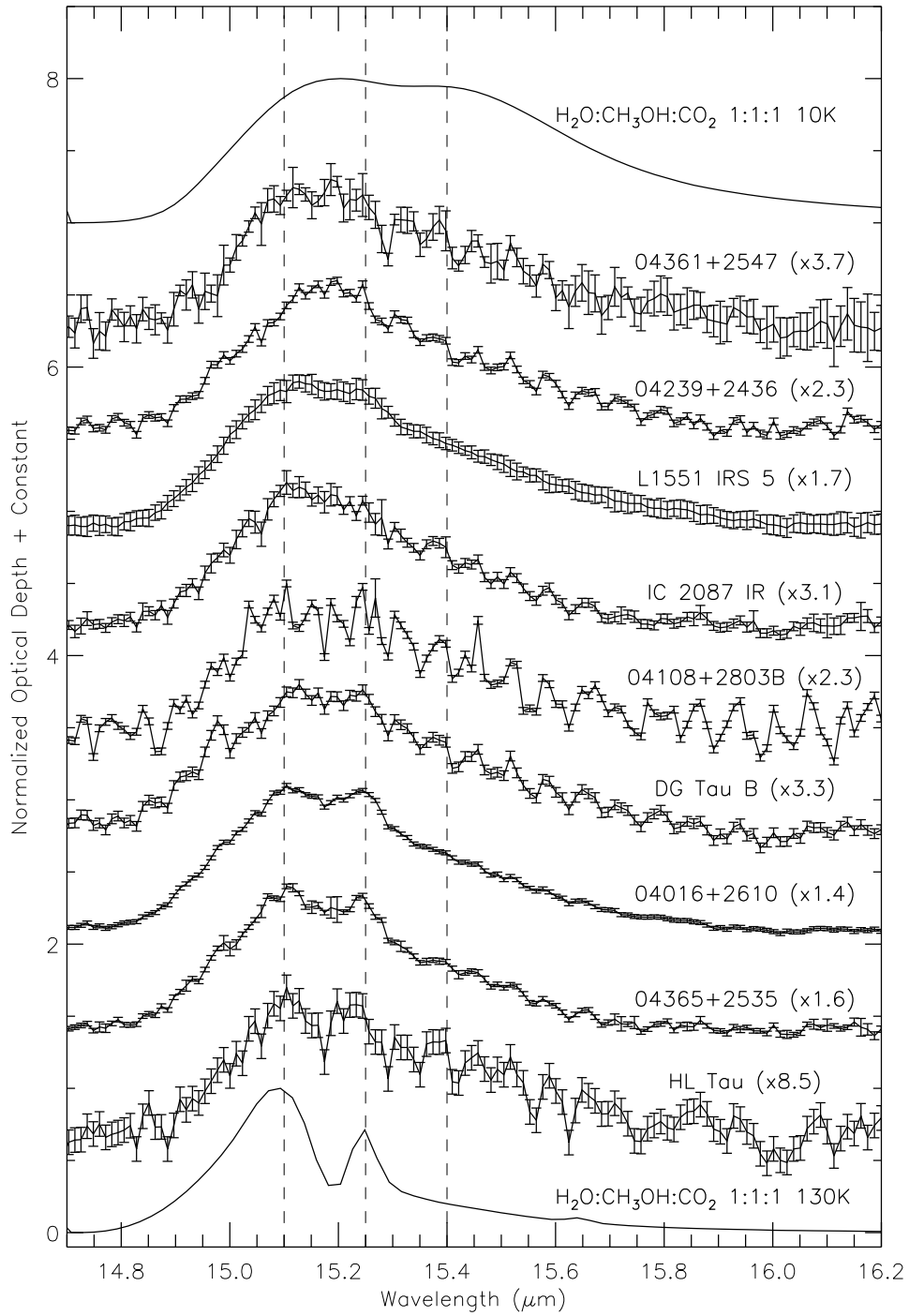


FIG. 14.— The high-resolution 15 μm Class I/II profiles visually ordered by “peakiness,” normalized to 1, and vertically offset for ease of plotting. The dotted lines at 15.1 μm and 15.25 μm mark the peak positions of pure CO_2 , and the one at 15.4 μm indicates the $\text{CH}_3\text{OH}:\text{CO}_2$ -complex shoulder. The top and bottom spectra are laboratory mixtures as indicated.

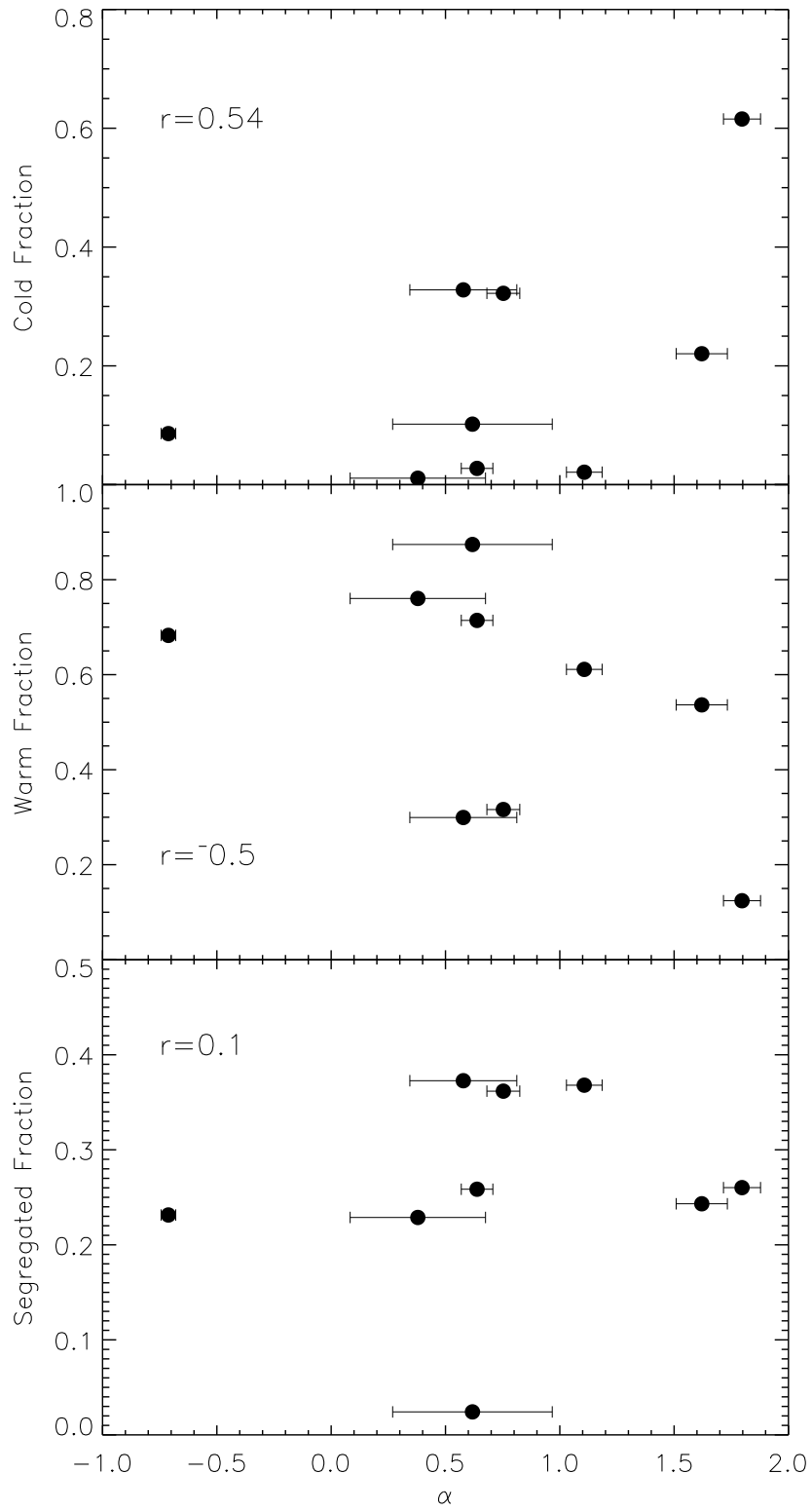


FIG. 15.— Relationship between SED 14.5-30 μm spectral index α and the CO₂ processing fractions in our Class I/II sample.

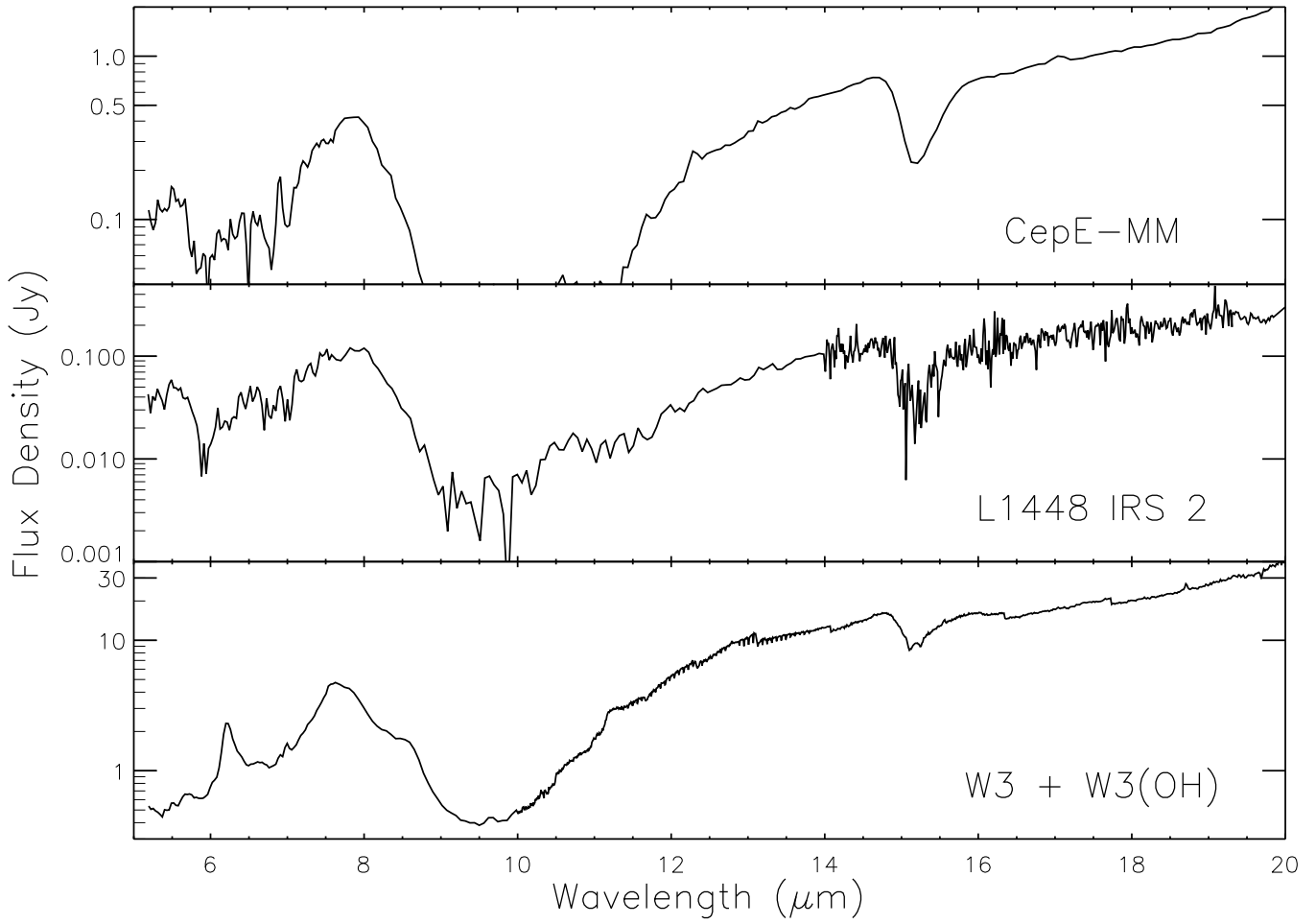


FIG. 16.— IRS spectra of the Class 0 protostars CepE-MM (Cepheus) and L1448 LRS 2 (Perseus), and the line of sight to W3(OH) through the W3 molecular cloud.

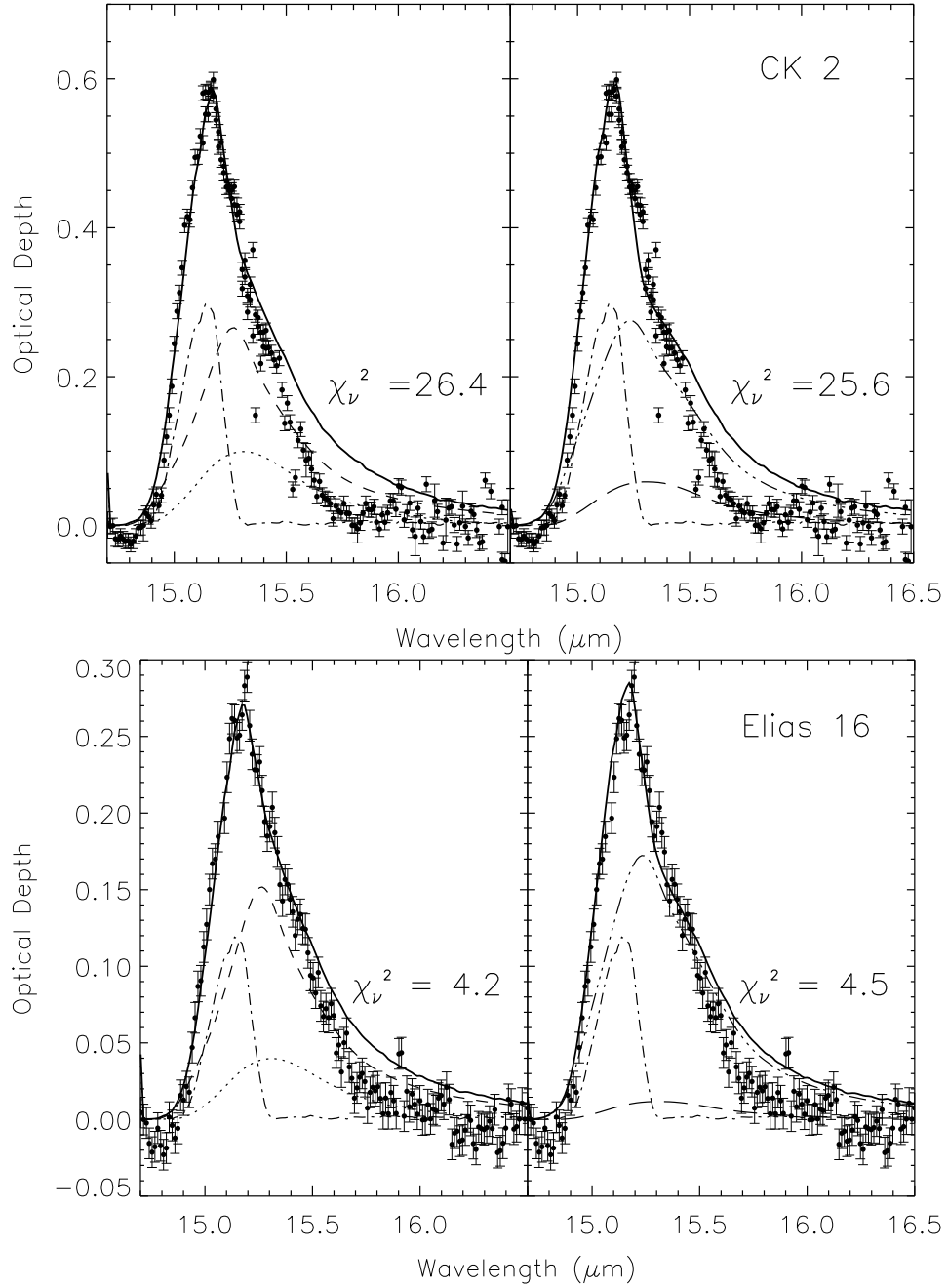


FIG. 17.— Comparison of fits to the Serpens background star CK 2 (top) and Taurus background star Elias 16 (bottom). The left panels are repeats of the fits by Knez et al. (2005), where the dotted line is a laboratory spectrum of $\text{H}_2\text{O}:\text{CO}_2$ 10:1 at 10K, the dashed line is $\text{H}_2\text{O}:\text{CO}_2$ 1:1 at 10K, and the dash-dot line is $\text{CO}:\text{N}_2:\text{CO}_2$ 10:5:2 at 30K. The mismatch on the red wing, compared with the published fit, is a result of our subtraction of the $13\ \mu\text{m}$ H_2O libration mode. In the right panels, the dash-dot line is the same, but the $\text{H}_2\text{O}:\text{CO}_2$ 10:1 spectrum has been replaced with $\text{H}_2\text{O}:\text{CH}_3\text{OH}:\text{CO}_2$ 9:2:1 at 30K (long dashes) and the $\text{H}_2\text{O}:\text{CO}_2$ 1:1 with $\text{H}_2\text{O}:\text{CH}_3\text{OH}:\text{CO}_2$ 0.9:0.3:1 at 30K (dash-triple dot).

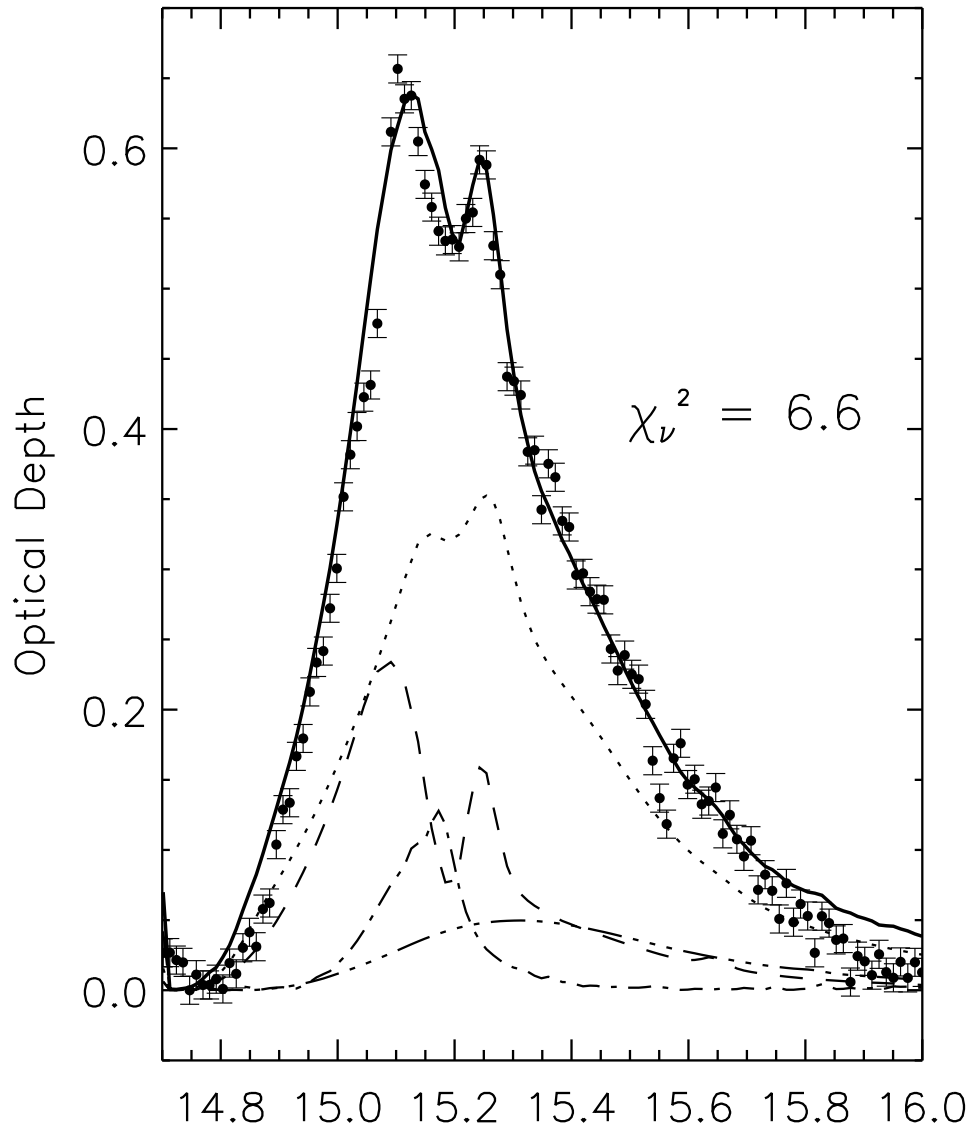


FIG. 18.— $15.2\ \mu\text{m}$ CO_2 feature probing W3(OH) and the foreground W3 cloud. It has been fitted with a combination of $\text{H}_2\text{O}:\text{CH}_3\text{OH}:\text{CO}_2$ 0.9:0.3:0.1 at 98K (dotted line), $\text{H}_2\text{O}:\text{CH}_3\text{OH}:\text{CO}_2$ 1:1:1 at 130K (dashed line), $\text{CO}:\text{H}_2\text{O}$ at 10:1 at 30K (dot-dashed line), and $\text{H}_2\text{O}:\text{CO}_2$ 10:1 (dash-triple dot). The solid line is the sum.